14. Kudo T, et al. (2009) Imaging of HIF-1-active tumor hypoxia using a protein effectively delivered to and specifically stabilized in HIF-1-active tumor cells. J Nucl Med, in press
15. Francis-Sedlak ME et al (2009) Characterization of type I collagen gels modified by glycation. Biomaterials 30(9):1851–1856
16. Zheng W et al (2008) Autofluorescence of epithelial tissue: single-photon versus two-photon excitation. J Biomed Opt 13(5):054010
17. Bassett AP et al (2004) Highly luminescent, triple- and quadruple-stranded, dinuclear Eu, Nd, and Sm(III) lanthanide complexes based on bis-diketonate ligands. J Am Chem Soc 126(30):9413–9424
18. Hasegawa Y et al (2000) Luminescence of novel neodymium sulfonylaminate complexes in organic media. Angew Chem Int Ed Engl 39(2):357–360
19. Gaft M et al (2008) Time-resolved laser-induced luminescence of UV-vis emission of Nd3+ in fluorite, scheelite and barite. J Alloys Compd 451(1–2):56–61
20. Hense BA et al (2008) Use of fluorescence information for automated phytoplankton investigation by image analysis. J Plankton Res 30(5):587–606
21. Brennan AM, Connor JA, Shuttleworth CW (2007) Modulation of the amplitude of NAD(P)H fluorescence transients after synaptic stimulation. J Neurosci Res 85(15):3233–3243
22. Kosterin P et al (2005) Changes in FAD and NADH fluorescence in neurosecretory terminals are triggered by calcium entry and by ADP production. J Membr Biol 208(2):113–124
23. Chen X, Conti PS, Moats RA (2004) In vivo near-infrared fluorescence imaging of integrin alphavbeta3 in brain tumor xenografts. Cancer Res 64(21):8009–8014
24. Hansch A et al (2004) In vivo imaging of experimental arthritis with near-infrared fluorescence. Arthritis Rheum 50(3):961–967
25. Mizukami S et al (1999) Imaging of caspase-3 activation in HeLa cells stimulated with etoposide using a novel fluorescent probe. FEBS Lett 453(3):356–360
26. Quici S et al (2004) New lanthanide complexes for sensitized visible and near-IR light emission: synthesis, 1H NMR, and X-ray structural investigation and photophysical properties. Inorg Chem 43(4):1294–1301
27. Zucchi G et al (2002) Highly luminescent, visible-emitting lanthanide macrocyclic chelates stable in water and derived from the cyclen framework. Inorg Chem 41(9):2459–2465
28. Amin S et al (1995) Laser-induced luminescence studies and crystal-structure of the europium(Iii) complex of 1, 4, 7, 10-tetrakis(carbamoylmethyl)-1, 4, 7, 10-tetraazacyclododecane - the link between phosphate diester binding and catalysis by lanthanide(Iii) macrocyclic complexes. Inorg Chem 34 (12):3294–3300
29. Livnah O et al (1993) Three-dimensional structures of avidin and the avidin-biotin complex. Proc Natl Acad Sci U S A 90 (11):5076–5080
30. Yao Z et al (1998) Avidin targeting of intraperitoneal tumor xenografts. J Natl Cancer Inst 90(1):25–29
31. Yao Z et al (1998) Imaging of intraperitoneal tumors with technetium-99 m GSA. Ann Nucl Med 12(2):115–118
32. Ouchi T et al (2004) Design of attachment type of drug delivery system by complex formation of avidin with biotinyl drug model and biotinyl saccharide. J Control Release 94(2–3):281–291

Research Article

LUMINESCENCE
The Journal of Biological and Chemical Luminescence

Received: 22 October 2008, Revised: 19 February 2009, Accepted: 1 February 2009 Published online in Wiley Interscience: 29 May 2009

(www.interscience.wiley.com) DOI 10.1002/bio.1136

NIR fluorescent ytterbium compound for *in vivo* fluorescence molecular imaging

Kazuki Aita[a,b], Takashi Temma[a], Yuji Kuge[a,c], Koh-ichi Seki[b] and Hideo Saji[a]*

ABSTRACT: We have developed a new NIR fluorescent probe based on an ytterbium(III) (*E*)-1-(pyridin-2-yl-diazenyl)naphthalen-2-ol (PAN) complex. This probe emits near-infrared luminescence derived from the Yb ion through excitation of the PAN moiety with visible light (λ_{ex} = 530 nm, λ_{em} = 975 nm). The results support the possible utility of the probe for *in vivo* fluorescence molecular imaging. Copyright © 2009 John Wiley & Sons, Ltd.

Keywords: ytterbium; near-infrared; energy transfer; fluorescence

Introduction

Molecular imaging is a rapidly emerging biomedical research field that may be defined as the visual representation, characterization and quantification of biological processes at the cellular and subcellular levels within a living organism.[1–3] As a molecular imaging technique, fluorescence imaging has attracted great interest, stimulating the development of more effective probes.

A potential probe for *in vivo* fluorescence imaging should emit light in the near-infrared (NIR) region (700–1000 nm). NIR light can permeate the body without intense absorbance or scatter by tissues,[4] and there is negligible self-fluorescence in the NIR region from living systems. In addition, a potential fluorescent probe should possess a large Stoke's shift to increase the signal-to-noise ratio. Provided that the Stoke's shift is large enough, scattered and reflected light derived from excitation light could be eliminated by appropriate filters. However, to the best of our knowledge, there are few reports of probes that fulfill the criteria of NIR fluorescence emission with a large Stoke's shift.

Some lanthanide (e.g. Eu, Tb, Nd, Yb, and Er) complexes that include an antenna moiety, a sensitizing chromophore, are well known as good fluorophores.[5–8] Their useful emission features, such as a large Stoke's shift (over 10 times larger than typical fluorescent dyes) and element-specific emission wavelength (visible in the IR region), have the potential for fluorescence imaging. Nd and Yb ions are especially suited for *in vivo* fluorescence imaging because of their NIR luminescence originating from $^4F_{3/2}$ to $^4I_{9/2}$ (at 870 nm) and $^2F_{5/2}$ to $^2F_{7/2}$ (at 975 nm) transitions, respectively.[9–11]

For these reasons, we aimed to develop a new fluorescent probe containing an ytterbium complex (Scheme 1). As a chelating moiety, 1,4,7,10-tetraazacyclododecane-1,4,7,10-tetraacetic acid (DOTA) was selected because DOTA and Yb^{3+} ion form a highly stable complex (the log K value of Yb^{3+} and $DOTA^{4-}$ is 25.81[12]) due to the tight coordination of DOTA with up to eight coordination sites. This implies that the complex would not be susceptible to metabolic degradation in living systems.[6] As an antenna moiety, (*E*)-1-(pyridin-2-yl-diazenyl)naphthalen-2-ol (PAN) was selected for three reasons. First, it is well known that PAN absorbs blue-green light (around 500 nm), which is harmless to living systems and reasonable for Yb excitation. Second, PAN is not fluorescent and has negligible fluorescence in the red to NIR region. Finally, the PAN structure does not contain pH-sensitive groups (carboxylic acid, primary amine, etc.). It was expected that a probe with these characteristics would display a high fluorescence yield and high *in vivo* stability.

In this study, we have synthesized PAN–DOTA(Yb), which includes the Yb–DOTA complex and PAN as a NIR fluorescent probe (Scheme 1), and have investigated its chemical and physical properties.

Materials and methods

Materials

All chemicals used in this study were commercial products of the highest purity and were further purified by standard methods, if necessary.

Instruments

FT-IR spectra were recorded with a Jasco FT/IR-4100 (Nihon Bunko Inc., Tokyo, Japan). UV–vis spectra were measured using a Hitachi U2001 (Hitachi High-Tech Manufacturing and Service Corporation, Ibaraki, Japan). ESI-MS measurements were performed on a Shimadzu LC-MS2010 EV (Shimadzu Corporation, Kyoto, Japan). ^{1}H-NMR spectra were recorded on a Jeol JNM-AL400 (Jeol Ltd, Tokyo, Japan). Fluorescence spectroscopy and quantum yield analysis were performed with a Fluorolog-3 (Horiba Jobin Yvon Inc., Kyoto, Japan). The slit width was 10 nm for both excitation and emission measurements.

* Correspondence to: H. Saji, Department of Patho-Functional Bioanalysis, Graduate School of Pharmaceutical Sciences, Kyoto University, Japan. E-mail: hsaji@pharm.kyoto-u.ac.jp

[a] Department of Patho-Functional Bioanalysis, Graduate School of Pharmaceutical Sciences, Kyoto University, Japan

[b] Central Institute of Isotope Science, Hokkaido University, Japan

[c] Department of Tracer Kinetics and Bioanalysis, Graduate school of Medicine, Hokkaido University, Japan

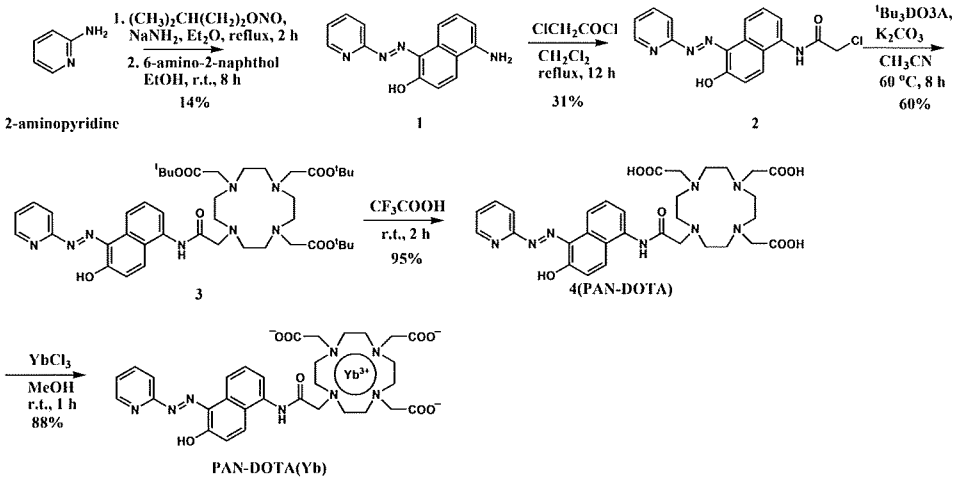

Scheme 1. Synthetic scheme for PAN-DOTA(Yb).

Fluorescence emission and excitation spectral measurements

The fluorescence emission spectra of PAN–DOTA(Yb) (10 μM) were measured in 10 mM Tris–HCl buffer (pH 8.0), 10 mM Britton–Robinson's buffer (pH 2.0–11.0), MeOH, EtOH and DMSO [each organic solvent contained 0.1% (v/v) Et_3N] at 25°C, following excitation at 530 nm. Excitation spectra were obtained at an emission wavelength of 975 nm.

Quantum yield analysis

The quantum yield analyses of PAN–DOTA(Yb) were measured by a previously reported method[13] in 10 mM Tris–HCl buffer (pH 8.0), MeOH, EtOH and DMSO [each organic solvent contained 0.1% (v/v) Et_3N] at 25°C, following excitation at 530 nm and emission at 975 nm. The reference compound [Yb(Tropolonate)$_4$] was measured at 380 nm excitation and 975 nm emission in 10 mM Tris–HCl buffer. The absorbance of the samples was adjusted to not exceed 0.2 at the excitation wavelength. The wavelength dependence of excitation light intensity and the detection efficiency of emission light were as given from Horiba Jobin Yvon Inc.

UV–visible absorption spectral measurements

The absorption spectral changes of PAN–DOTA and PAN–DOTA(Yb) (10 μM) in 10 mM Tris–HCl buffer (pH 8.0) at 25°C were determined.

Synthesis

(*E*)-1-(pyridin-2-yl-diazenyl)-5-amino-naphthalen-2-ol (PAN–NH_2). To a solution of 2-amino-pyridine (940 mg, 10.0 mmol) in dry THF (50 mL) was added sodium amide (390 mg, 10.0 mmol) under a slight flow of nitrogen gas. Vigorous stirring was maintained at 40°C. After ammonia evolution had ceased, isopentylnitrate (1.01 g, 10.0 mmol) was added and stirring was continued for another hour under a nitrogen atmosphere at 40°C. The precipitated sodium diazotate was filtered, washed with Et_2O and immediately dissolved in cold, dry THF (30 mL). The THF solution of sodium diazotate was added to a solution of 5-amino-2-naphthol (1.59 g, 10.0 mmol) in THF (30 mL), and with carbon dioxide gas bubbling. The resulting solution was concentrated by evaporation. PAN–NH_2 was isolated by silica gel column chromatography (diameter = 3 cm, column length = 20 cm, eluent $CHCl_3$:MeOH = 10:1). The desired fractions were collected and concentrated by evaporation. The resulting powder was dried under vacuum to obtain PAN–NH_2 (370 mg, 1.4 mmol, 14%) as a reddish brown powder.

MS (ESI, pos.) *m/z* found 265 ([M + H]$^+$), calcd 265 ^{1}H-NMR (400 MHz, CD_3OD) δ 8.55 (1H, d, J = 1.0 Hz), 8.27 (1H, d, J = 1.0 Hz), 8.05 (1H, d, J = 8.6 Hz), 7.97–7.86 (2H, m), 7.74 (1H, d, J = 9.0 Hz), 7.38–7.34 (1H, m), 7.02 (1H, t, J = 10.5 Hz), 6.61 (1H, d, J = 8.8 Hz).

(*E*)-1-(pyridin-2-yl-diazenyl)-5-amidochloromethyl-naphthalen-2-ol (PAN–Cl). PAN–NH_2 (528 mg, 2.0 mmol) was dissolved in dry THF (20 mL). To the solution was added a solution of $ClCH_2COCl$ (250 mg, 2.2 mmol) dissolved in dry THF (10 mL), causing the solution to become black. The mixture was stirred for 5 h at room temperature and then concentrated by evaporation. PAN–Cl was isolated by silica gel column chromatography (diameter = 3 cm, column length = 20 cm, eluent $CHCl_3$:MeOH = 10:1). The desired fractions were collected and concentrated by evaporation. The resulting powder was dried under vacuum to obtain PAN–Cl (211 mg, 0.6 mmol, 31%) as a yellow powder.

MS (ESI, pos.) *m/z* found 341 ([M + H]$^+$), calcd 341. ^{1}H-NMR (400 MHz, CD_3OD) δ 8.56 (1H, ddd, J = 0.9, 1.9, 4.9 Hz), 8.27 (1H, d, J = 2.6 Hz), 8.06 (1H, d, J = 8.7 Hz), 7.99–7.94 (2H, m), 7.88 (1H, td, J = 1.3, 8.0 Hz), 7.37 (1H, ddd, J = 1.1, 5.2, 7.4 Hz), 7.04 (1H, dd, J = 2.6, 9.1 Hz), 6.63 (1H, d, J = 8.7 Hz), 4.15 (2H, s).

1-[(*E*)-1-(pyridin-2-yl-diazenyl)-5-amidomethyl-naphthalen-2-ol]-1,4,7,10-tetraazacyclododecane-4,7,10-triacetic acid tri-*tert*-butyl ester (PAN-^{t}Bu$_3$DOTA). A dry DMF suspension (10 mL) of 1,4,7,10-tetraazacyclododecane-1,4,7-triacetic acid tri-*tert*-butyl ester (^{t}Bu$_3$DO3A) (51.5 mg, 0.1 mmol), K_2CO_3 (138 mg, 1.0 mmol) and KI (166 mg, 1.0 mmol) was stirred for 5 min at 60°C under anaerobic conditions. To the suspension was then slowly added a solution of PAN–Cl (34.0 mg, 0.1 mmol) in dry DMF (10 mL). After stirring for 13 h at 60°C, the suspension was filtered and the residue was washed with MeCN. This residue was added to MeOH (20 mL), stirred for 30 min to give a reddish suspension which was filtered and washed with MeOH. The filtrate was

LUMINESCENCE
The Journal of Biological and Chemical Luminescence

concentrated by evaporation. PAN-^{t}Bu$_3$DOTA was isolated by silica gel column chromatography (diameter = 1.5 cm, column length = 15 cm, eluent $CHCl_3$:MeOH = 10:1). The desired fractions were collected and concentrated by evaporation. The resulting powder was dried under vacuum to obtain PAN-^{t}Bu$_3$DOTA (49.0 mg, 60 μmol, 60%) as a red powder.

MS (ESI, pos.) *m/z* found 819 ($[M + H]^+$), calcd 819. ^{1}H-NMR (400 MHz, $CDCl_3$) δ 8.27 (1H, dd, J = 3.3, 8.3 Hz), 7.65 (1H, d, J = 8.5 Hz), 7.56 (1H, d, J = 7.4 Hz), 7.43 (1H, d, J = 7.9 Hz), 7.36-7.23 (4H, m), 6.66 (1H, d, J = 9.9 Hz), 3.82 (6H, s), 3.71 (2H, s), 3.32–2.79 (16H, br), 1.43 (27H, s).

1-[(*E*)-1-(pyridin-2-yl-diazenyl)-5-amidomethyl-naphthalen-2-ol]-1,4,7,10-tetraazacyclododecane-4,7,10-triacetic acid (PAN-DOTA). PAN-^{t}Bu$_3$DOTA (41.0 mg, 50 μmol) was dissolved in trifluoroacetic acid (5.0 mL) at 0°C. After stirring for 1 h at 0°C, the resulting solution was poured into Et_2O (50 mL), and filtered. The residue was washed with Et_2O three times, and the resulting powder was dried under vacuum to obtain PAN-DOTA (30.8 mg, 48 μmol, 95%) as a reddish yellow powder.

MS (ESI, neg.) *m/z* found 649 ($[M - H]^-$), calcd 649. ^{1}H-NMR (400 MHz, CD_3OD) δ 7.94 (1H, d, J = 7.9 Hz), 7.61 (1H, d, J = 7.1 Hz), 7.49 (1H, d, J = 8.7 Hz), 7.34 (2H, t, J = 7.9 Hz), 7.25 (1H, t, J = 7.9 Hz), 7.12-7.10 (3H, m), 3.92 (8H, br), 3.20–3.04 (16H, br).

PAN-DOTA(Yb)

To an MeOH solution (2 mL) containing PAN-DOTA (6.5 mg, 10 μmol) was added $YbCl_3$ $6H_2O$ (3.9 mg, 10 μmol) in MeOH solution (2 mL). After stirring for 1 h at room temperature, the resulting solution was poured into Et_2O (10 mL), and filtered. The residue was washed with Et_2O three times, and the resulting powder was dried under vacuum to obtain PAN-DOTA(Yb) (7.2 mg, 8.8 μmol, 88%) as a red powder. MS(ESI, pos.) *m/z* found 822 ($[M - H]^-$), calcd. 822.

Results

Synthesis of PAN-DOTA(Yb)

PAN-DOTA was synthesized from 2-aminopyridine in four steps, as shown in Scheme 1, and the overall yield from starting material was 2.5%. PAN-DOTA(Yb) was synthesized by stirring PAN-DOTA and $YbCl_3$ in MeOH with the yield of 88%. Other lanthanide complexes, PAN-DOTA(Ln) (Ln = Eu, Tb and Nd), were similarly prepared from $EuCl_3$, $TbCl_3$ and $NdCl_3$ with the yields of 90, 85 and 92%, respectively.

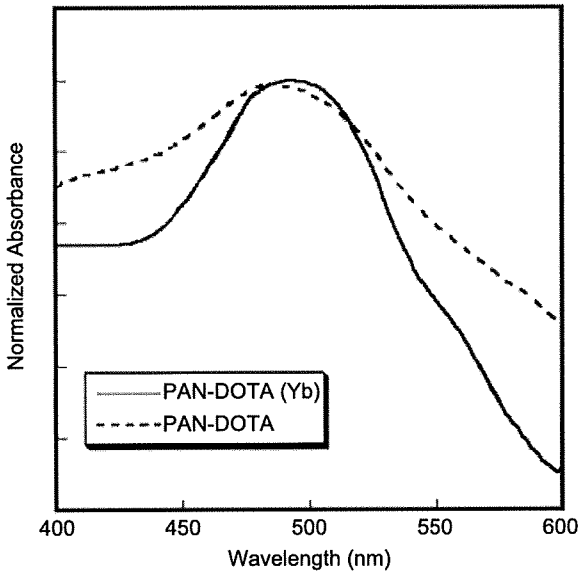

Figure 1. UV-vis absorption spectra of PAN-DOTA (dotted line) and PAN-DOTA(Yb) (solid line).

Spectroscopic characterizations of PAN-DOTA(Yb) in aqueous solution

In the IR spectra, carbonyl C=O stretching absorptions were observed at 1732 cm^{-1} for PAN-DOTA and 1717 cm^{-1} for PAN-DOTA(Yb), and amide N-H bending absorptions were found at 1569 cm^{-1} for PAN-DOTA and 1559 cm^{-1} for PAN-DOTA(Yb) (data not shown).

UV-vis spectra of aqueous solutions of PAN-DOTA(Yb) and PAN-DOTA are shown in Fig. 1. The maximal absorption wavelengths were 490 nm [PAN-DOTA(Yb)] and 480 nm (PAN-DOTA), respectively.

The emission spectra of aqueous solutions of PAN-DOTA(Yb), PAN-DOTA, $YbCl_3$ and DOTA(Yb) are shown in Fig. 2(A). A sharp and strong peak at 975 nm was detected only in the PAN-DOTA(Yb) spectrum (λ_{ex} = 530 nm). In contrast, no fluorescence

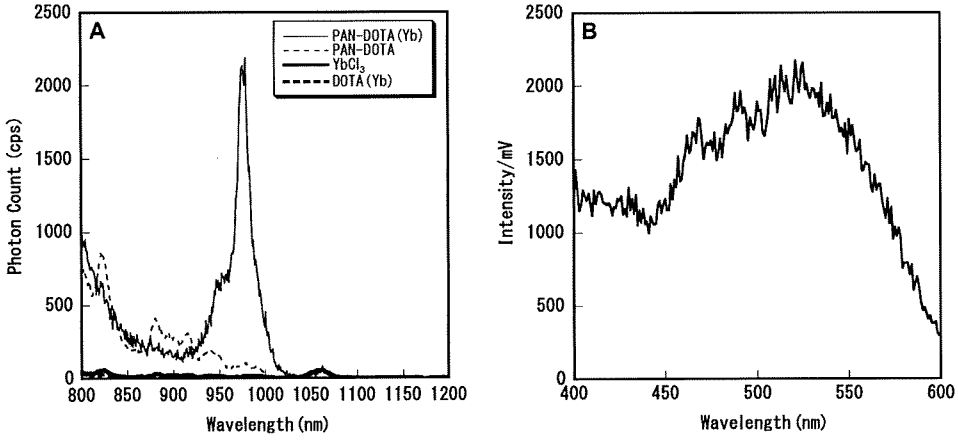

Figure 2. Spectroscopy data for PAN-DOTA (dotted line), PAN-DOTA(Yb) (solid line), $YbCl_3$ (solid and bold line) and DOTA(Yb) (dotted and bold line). (A) Emission spectra (λ_{ex} = 530 nm). (B) Excitation spectra (λ_{em} = 975 nm).

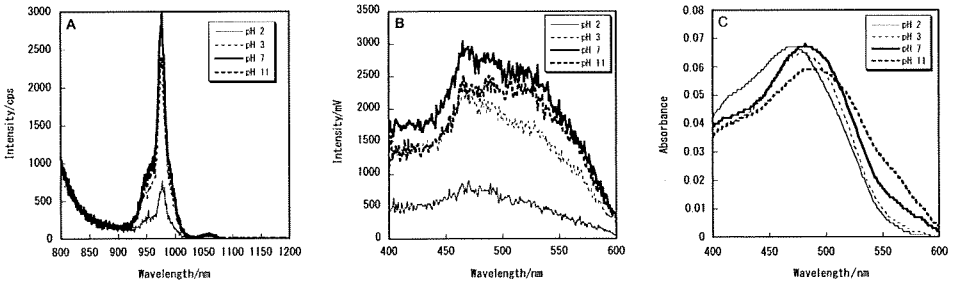

Figure 3. pH effect on spectral features of PAN-DOTA(Yb). (A) Emission spectra (λ_{ex} = 530 nm). (B) Excitation spectra (λ_{em} = 975 nm). (C) UV-vis absorption spectra. Spectra show the results at pH 2.0 (solid line), pH 3.0 (dotted line), pH 7.0 (solid and bold line) and pH 11.0 (dotted and bold line).

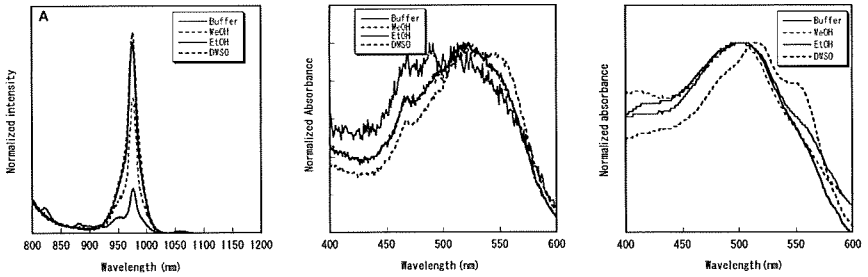

Figure 4. Solvent effects on spectral features of PAN-DOTA(Yb). (A) Emission spectra (λ_{ex} = 530 nm). (B) Excitation spectra (λ_{em} = 975 nm). (C) UV-vis absorption spectra. Spectra were measured in buffer (solid line), MeOH (dotted line), EtOH (solid and bold line) and DMSO (dotted and bold line).

peak was detected for PAN–DOTA, $YbCl_3$ or DOTA(Yb) under the same conditions.

Figure 2(B) shows the excitation spectrum of an aqueous solution of PAN–DOTA(Yb) (λ_{em} = 975 nm). The wavelength maxima was at 530 nm while an overtone of the detection light somewhat affected the shape of the curve around 490 nm.

PAN–DOTA complexes with other lanthanides gave differing fluorescence spectra. PAN–DOTA(Nd) showed a small peak at approximately 880 nm due to a typical neodymium $^4F_{3/2}$ to $^4I_{9/2}$ transition upon excitation with 530 nm light. PAN–DOTA(Eu) and PAN–DOTA(Tb) had no emission peaks from excitation at 530 nm in part because of the higher energy levels required to excite Eu and Tb.

Effects of pH and solvent on the fluorescence of PAN–DOTA(Yb)

The effect of pH on the fluorescence of PAN–DOTA(Yb) was examined [Fig. 3(A)]. The fluorescence intensity of PAN–DOTA(Yb) remained constant in the pH 3–11 range; however, it was weak at pH 2. Similarly, the excitation spectra [Fig. 3(B)] and the UV–vis absorption spectra [Fig. 3(C)] also showed that the energy levels of PAN–DOTA(Yb) were almost constant from pH 3 to 11. In addition, in the pH 2–11 range, no degradation products were detected by electrospray ionization mass spectrometry (ESI-MS) analysis.

PAN–DOTA(Yb) could be dissolved in several polar organic solvents. Figure 4 shows the emission [Fig. 4(A)], excitation [Fig. 4(B)] and UV–vis absorption [Fig. 4(C)] spectra of PAN–DOTA(Yb) in 10 mM Tris–HCl buffer (pH 8.0) and the organic solvents MeOH, EtOH and DMSO.

The λ_{max} of the excitation wavelength that gives a 975 nm emission changed slightly around 520 nm in the three tested organic solvents [Fig. 4(B)]. On the other hand, the emission spectra showed the exact same λ_{max} in the four tested solvents while the fluorescence intensity changed [Fig. 4(A)].

Table 1. Quantum yields of PAN–DOTA(Yb) and $[Yb(tropolonate)_4]^-$

Complex	Solvent	Quantum yield
PAN–DOTA(Yb)	0.01 M Tris buffer (pH 8.0)	8.6×10^{-5}
PAN–DOTA(Yb)	MeOH[a]	1.8×10^{-4}
PAN–DOTA(Yb)	EtOH[a]	3.5×10^{-4}
PAN–DOTA(Yb)	DMSO[a]	5.4×10^{-4}
$[Yb(Tropolonate)_4]^-$	0.01 M Tris buffer (pH 8.0)	2.4×10^{-4}[b]

[a]Contains 0.1% (v/v) Et_3N.
[b]This value is from Zhang *et al.*[13]

Quantum yield analysis

Quantum yields (Φ) of PAN–DOTA(Yb) were measured in several solvents using $[Yb(Tropolonate)_4]^-$ ($\Phi = 2.4 \times 10^{-4}$ in 0.01 M TRIS buffer[13]) as a standard. Table 1 shows the quantum yields of PAN–DOTA(Yb) to be 8.6×10^{-5}, 1.8×10^{-4}, 3.5×10^{-4} and 5.4×10^{-4} as measured at room temperature in Tris buffer (pH 8.0), MeOH, EtOH and DMSO, respectively.

Discussion

In IR spectra, the peak shifts with the Yb chelation suggest that the three carbonyl and one amide groups of the DOTA moiety participate in chelation of the Yb ion. In UV–vis absorption spectra (Fig. 1), the wavelength maxima changed slightly after metal chelation. Since it was previously reported that the maximal

LUMINESCENCE
The Journal of Biological and Chemical Luminescence

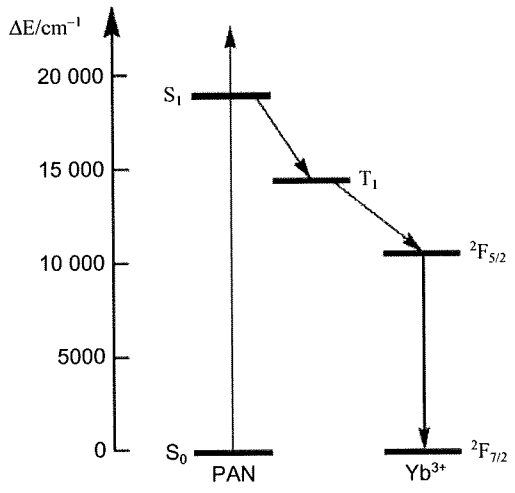

Figure 5. Simple photophysical scheme describing a possible pathway for sensitization of Yb luminescence in PAN-DOTA(Yb).

absorption wavelength was shifted to around 560 nm by chelation with the zinc ion,[14] these data indicate that the DOTA chelation of Yb ion does not have a major effect on the energy level of the PAN moiety.

A sharp and strong emission peak at 975 nm detected in the PAN–DOTA(Yb) emission spectrum (λ_{ex} = 530 nm) can be assigned to a typical Yb $^2F_{5/2}$ to $^2F_{7/2}$ transition. The emission feature disappeared with the lack of PAN moiety or Yb ion. These results suggest that the 975 nm luminescence shown in PAN–DOTA(Yb) is derived from energy transfer from an excited PAN moiety to the Yb fluorescent center.

PAN–DOTA(Yb) emits NIR fluorescence through its excitation by visible light with a very large Stoke's shift, as expected. These features are similar to our previous compound [4AMF-DOTA(Nd)], which has a fluorescence at 880 nm from excitation by 488 nm light.[15]. In addition, an undesirable fluorescence around 525 nm from the antenna moiety present in 4AMF-DOTA(Nd) was eliminated by using a non-fluorescent antenna moiety in PAN–DOTA(Yb). The peak fluorescent counts originating from lanthanide were measured to be 2188 [PAN–DOTA(Yb), λ_{em} = 975 nm] and 2220 [4AMF-DOTA(Nd), λ_{em} = 880 nm], and the noise fluorescent counts not originating from lanthanide (λ_{em} = 800 nm) were 1038 [PAN–DOTA(Yb)] and 4786 [4AMF-DOTA(Nd)]. Therefore, the signal-to-noise ratios were 2.10 [PAN–DOTA(Yb)] and 0.46 [4AMF-DOTA(Nd)]. These data indicate that PAN–DOTA(Yb) could be superior to 4AMF-DOTA(Nd) for *in vivo* fluorescence molecular imaging with an expected increase in signal-to-noise ratio.

Although the mechanism of energy transfer from the PAN moiety to Yb ion is still unclear, the triplet excitation state of the antenna moiety might participate in this process.[16] A simple model of this process is depicted in Fig. 5.

PAN–DOTA(Yb) had a stable fluorescent feature over a wide pH range (pH 3–11). In contrast, we reported previously that the fluorescence from 4AMF–DOTA(Nd) disappeared at pH < 5.0 due to its pH-sensitive functional groups. Thus, PAN–DOTA(Yb), with a more favorable pH fluorescence profile, is considered to be superior to 4AMF–DOTA(Nd) as a probe, especially for *in vivo* applications. In addition, the high stability from the decomposition in solution indicate that PAN–DOTA(Yb) could be widely employed as a fluorescence imaging probe in pH-fluctuating environments.

Even though the excitation peak of PAN–DOTA(Yb) was slightly changed by the solvent, the emission peak was not susceptible to environmental changes, not only the pH but also the solvent. The lack of solvent effect on emission wavelength is due to a characteristic of lanthanide ions in which the 5s and 5d orbitals are located outside the 4f orbital responsible for fluorescence, resulting in protection from environmental influences. These data further support the notion of the observed fluorescence around 975 nm being derived from the Yb ion. PAN–DOTA(Yb) displayed a stronger emission intensity in organic solvents than in buffer, probably because H_2O can act as a quencher for excited PAN–DOTA(Yb) in some processes.

These quantum yield values are slightly diminished as compared with other Yb complexes reported previously.[13,17,18] This effect may partially reflect differences in structure, in particular, the distance between the chromophore (PAN moiety) and the fluorophore [DOTA(Yb) moiety]. In many reports, the Yb ion was directly coordinated by the chromophore, but in the case of PAN–DOTA(Yb), the PAN moiety does not coordinate to the Yb, as indicated by small change in the UV–vis spectrum after Yb complexation. Thus, the energy transfer ratio from the PAN moiety to DOTA(Yb) would be lower than for directly coordinated complexes. While most of the previously reported complexes tend to be influenced by their surroundings, PAN–DOTA(Yb), because of the structural independence of fluorescent center and antenna moiety, has a stable fluorescence under many conditions.

As expected, PAN–DOTA(Yb) shows higher quantum yields in organic solvents than in buffer [Fig. 4(A)]. This is a common feature of many lanthanide (e.g. Nd^{3+}, Yb^{3+}, Er^{3+}) complexes because the luminescence from lanthanide ions is susceptible to vibratory quenching by O–H oscillators.

Conclusion

The results obtained in this study indicate that PAN–DOTA(Yb) has the potential for *in vivo* fluorescence imaging with several favorable properties, such as near-infrared luminescence, visible light excitation, and a large Stoke's shift. In addition, a negligible fluorescence from the PAN moiety and pH-stability are other potential advantages of PAN–DOTA(Yb).

References

[1] Fu G, Yang HY, Wang C, Zhang F, You ZD, Wang GY, He C, Chen YZ, Xu ZZ. Detection of constitutive heterodimerization of the integrin Mac-1 subunits by fluorescence resonance energy transfer in living cells. Biochem Biophys Res Commun 2006;346:986–91.
[2] Wandelt B, Cywinski P, Darling GD, Stranix BR. Single cell measurement of micro-viscosity by ratio imaging of fluorescence of styrylpyridinium probe. Biosens Bioelectron 2005;20:1728–36.
[3] Mizukami S, Kikuchi K, Higuchi T, Urano Y, Mashima T, Tsuruo T, Nagano T. Imaging of caspase-3 activation in HeLa cells stimulated with etoposide using a novel fluorescent probe. FEBS Lett 1999;453:356–60.
[4] Konig K. Multiphoton microscopy in life sciences. J Microsc 2000;200:83–104.
[5] Colette S, Amekraz B, Madic C, Berthon L, Cote G, Moulin C. Europium(III) interaction with a polyaza-aromatic extractant studied by time-resolved laser-induced luminescence: a thermodynamical approach. Inorg Chem 2004;43:6745–51.
[6] Quici S, Marzanni G, Forni A, Accorsi G, Barigelletti F. New lanthanide complexes for sensitized visible and near-IR light emission: synthesis, 1HnmR, and X-ray structural investigation and photophysical properties. Inorg Chem 2004;43:1294–301.
[7] Gunnlaugsson T, MacDonaill DA, Parker D. Lanthanide macro-cyclic quinolyl conjugates as luminescent molecular-level devices. J Am Chem Soc 2001;123:12866–76.

[8] Werts MHV, Hofstraat JW, Geurts FAJ, Verhoeven JW. Fluorescein and eosin as sensitizing chromophores in near-infrared luminescent ytterbium(III), neodymium(III) and erbium(III) chelates. Chem Phys Lett 1997;276:196–201.
[9] Faulkner S, Carrie MC, Pope SJ, Squire J, Beeby A, Sammes PG. Pyrene-sensitised near-IR luminescence from ytterbium and neodymium complexes. Dalton Trans 2004:1405–9.
[10] Beer PD, Szemes F, Passaniti P, Maestri M. Luminescent ruthenium(II) bipyridine-calix[4]arene complexes as receptors for lanthanide cations. Inorg Chem 2004;43:3965–75.
[11] Hasegawa Y, Ohkubo T, Sogabe K, Kawamura Y, Wada Y, Nakashima N, Yanagida S. Luminescence of novel neodymium sulfonylaminate complexes in organic media. Angew Chem Int Ed Engl 2000;39:357–60.
[12] Wu SL, Horrocks WD. Direct determination of stability constants of lanthanide ion chelates by laser-excited europium(III) luminescence spectroscopy: application to cyclic and acyclic aminocarboxylate complexes. *J* Chem Soc Dalton Trans 1997:1497–502.
[13] Zhang J, Badger PD, Geib SJ, Petoud S. Sensitization of near-infrared-emitting lanthanide cations in solution by tropolonate ligands. Angew Chem Int Ed Engl 2005;44:2508–12.
[14] Malik AK, Sharma V, Sharma VK, Rao AL. Column preconcentration and spectrophotometric determination of ziram and zineb in commercial samples and foodstuffs using (1,2′-pyridylazo)-2-naphthol (PAN)-naphthalene as adsorbate. J Agric Food Chem 2004;52:7763–7.
[15] Aita K, Temma T, Kuge Y, Saji H. Development of a novel neodymium compound for *in vivo* fluorescence imaging. Luminescence 2007;22:455–61.
[16] Crosby GA, Alire RM, Whan RE. Intramolecular energy transfer in rare earth chelates—role of triplet state. J Chem Phys 1961;34:743–8.
[17] Foley TJ, Harrison BS, Knefely AS, Abboud KA, Reynolds JR, Schanze KS, Boncella JM. Facile preparation and photophysics of near-infrared luminescent lanthanide(III) monoporphyrinate complexes. Inorg Chem 2003;42:5023–32.
[18] Zhang J, Petoud S. Azulene-moiety-based ligand for the efficient sensitization of four near-infrared luminescent lanthanide cations: Nd^{3+}, Er^{3+}, Tm^{3+}, and Yb^{3+}. Chemistry 2008;14:1264–72.


不安定性動脈硬化プラークイメージングのための分子プローブ開発研究

京都大学大学院薬学研究科病態機能分析学分野　天満　敬、佐治英郎

1．はじめに

近年、動脈内のプラーク破綻とそれに伴う血栓形成が心筋梗塞や脳梗塞の発症に深く関与していることが明らかとなり、動脈内のプラークの不安定性を精度よく評価できる診断法の開発が切望されている。これまでに、超音波診断法、MRI、X線CT等を用いた検討が行われているが、未だ形態的検討が主で、質的診断に有効な方法は開発されていない[1]。一方、PET、SPECTを用いる核医学分子イメージング法は、生体内機能分子をインビボで非侵襲的かつ定量的に画像化できるため、動脈硬化プラークの不安定化に関与する機能分子を標的とする分子プローブを用いることで動脈硬化の質的診断への応用が期待されている。本稿では、我々の研究室において実施された不安定性動脈硬化プラークイメージングに関する研究の概略を紹介したい。

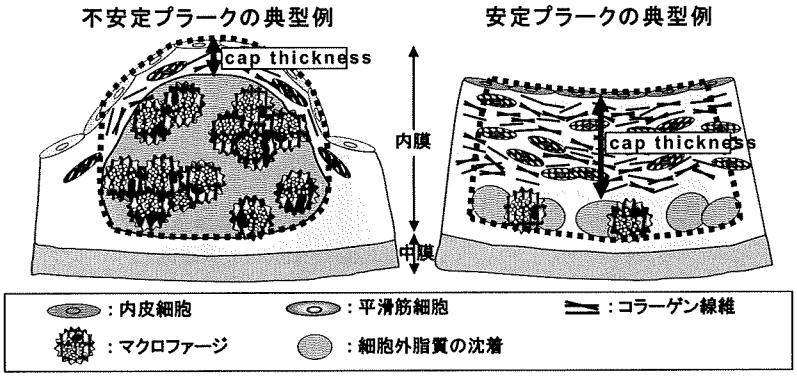

図1　不安定プラーク（左）、安定プラーク（右）の典型例

1．不安定性動脈硬化プラークとは

不安定性動脈硬化プラークの特徴として、①脂質に富む柔らかな粥腫があること②線維性被膜が脆弱化していること③マクロファージなどの炎症性細胞が浸潤していること、が挙げられる。一方、安定プラークでは線維性組織が発達し内膜の肥厚は認められるものの、マクロファージの浸潤はほとんど無い[7-10]（図1）。

2．^{18}F-FDG

不安定性動脈硬化プラークの特徴のひとつにマクロファージの存在がある。そこで、マクロファージではエネルギー代謝が活発であり、そのエネルギー源として糖（グルコース）を用いていることに着目し、糖代謝イメージング剤である^{18}F-FDGを用いた不安定プラークイメージングが試みられてきている。当研究室においては、不安定性動脈硬化プラークへの^{18}F-FDGの集積を基礎的に検討するために、動脈硬化モデル動物であるWatanabe heritable hyperlipidemic (WHHL)ウサギに^{18}F-FDGを投与し、マクロファージ浸潤度と放射能集積量の関連、PETを用いたイメージング検討を行った[2]。その結果、^{18}F-FDGは対照群であるNZWウサギの血管に比較してWHHLウサギの血管へ有意に高く集積し、また、その集積量はマクロファージ数と高い相関を示すことを見出した（図2A）。一方、内膜の肥厚度と放射能集積量との間には相関は認められなかった（図2B）。このことから、^{18}F-FDGの集積には安定プラークでも認められる内膜の肥厚度ではなく、不安定プラークで特異的に増加しているマクロファージが関与していることを示した。さらに、PET撮像により、動脈硬化病変を示す大動脈血管を^{18}F-FDG投与3~4時間後に明確に描出できた（図2C, D）。これらの結果は、^{18}F-FDGが不安定プラークを描出することの科学的基盤を与えた。さらに、不安定プラークの薬物治療効果の評価は、治療方針決定や新しい治療薬開発に有効であることから、

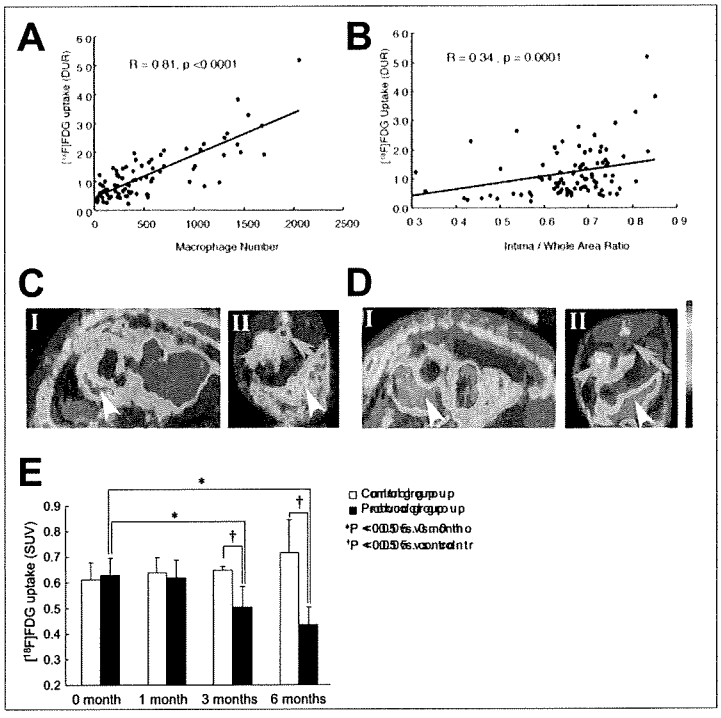

図2 [2, 3] (A) ^{18}F-FDG集積とマクロファージ数との関連
(B) ^{18}F-FDG集積と内膜肥厚度との関連(C) PET/CT画像-WHHLウサギ
(D) PET/CT画像-NZWウサギ　矢（オレンジ）、矢じり（オレンジ）、矢じり（白）はそれぞれ動脈、腎臓、肝臓を示す
(E) 薬剤治療による^{18}F-FDG集積変化

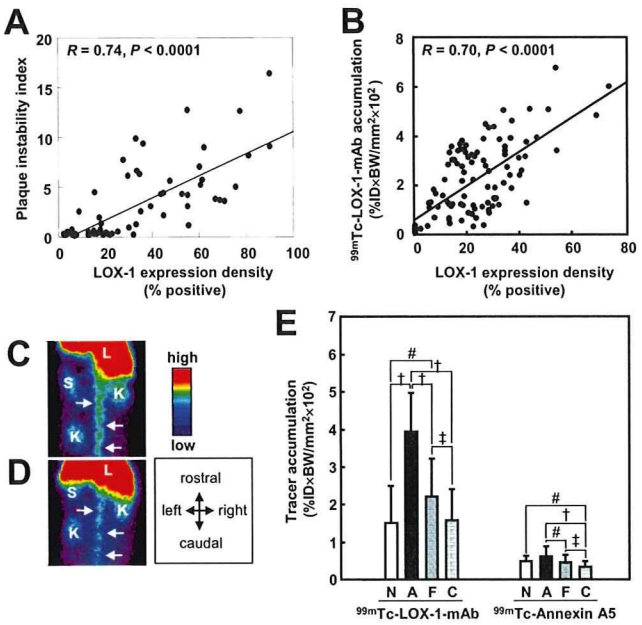

図3 [4-6] **(A) LOX-1発現量とプラーク不安定性との関連 (B) LOX-1発現量と^{99m}Tc標識抗LOX-1抗体集積との関連 (C) プラナー画像-WHHLウサギ (D) プラナー画像-JWウサギ 白矢印、L、S、Kはそれぞれ動脈、肝臓、脾臓、腎臓を示す (E) ^{99m}Tc標識抗LOX-1抗体と^{99m}Tc標識annexin A5の病変集積量比較（†P<0.0001, #P<0.005, ‡P<0.01）N、A、F、Cはそれぞれ新生内膜病変、アテローム性病変（不安定プラーク）、フィブロアテローム性病変、コラーゲンリッチ病変である**

^{18}F-FDG－PET法の薬物治療評価への応用可能性を検討した[3]。すなわち、myocardial infarction-prone WHHL (WHHLMI)ウサギに動脈硬化治療薬であるプロブコールを含む餌を与え、^{18}F-FDGの放射能集積変化を経時的に調べた。その結果、血管への放射能集積が薬剤投与3ヵ月後から減少し、6ヶ月後には血管が描出されなくなった（図2E）。これにより、^{18}F-FDG－PET法が不安定プラークにおける薬物治療評価に有効であることを示した。

3. スカベンジャー受容体イメージング

糖代謝亢進を集積原理とする^{18}F-FDGは、元来エネルギー活動の活発な心筋に高く集積し、動脈硬化病変の好発部位である冠動脈への適用は困難という問題点がある。また、^{18}F-FDGは初期の動脈硬化病変にも集積することから、新たに、疾患の進行度を評価可能な不安定プラークの質的診断用イメージングプローブの開発が求められている。

そこで我々は、動脈硬化プラークの不安定化に関与する、血管内皮細胞への炎症細胞の接着促進、マクロファージの泡沫化促進、コラーゲン線維の分解などに重要な役割を果たす可能性が細胞を用いた実験結果から示されている、酸化LDL受容体ファミリーの一つであるLectin-like oxidized LDL receptor-1 (LOX-1)を不安定プラークイメージングの標的分子として着目した。組織学的検討により、LOX-1の発現はプラークの不安定性の指標と高い相関を示し、LOX-1が標的分子として有効であることを見出した（図3A）[4,11]。そこで次に、LOX-1イメージング剤として^{99m}Tc標識抗LOX-1抗体の開発を計画し、二官能性キレートという分子設計概念に基づいて^{99m}Tc標識抗LOX-1抗体を合成し、その体内分布挙動をWHHLMIウサギを用いて検討した結果[5]、血管への放射能集積はLOX-1の発現量、および、プラークの不安定性の指標と高く相関することを見出した（図3B）。また、開発した^{99m}Tc標識抗LOX-1抗体を用いて投与24時間後に核医学イメージングを行った結果、コントロールウサギではほとんど大動脈が描出されないのに対して、WHHLMIウサギでは明瞭に大動脈が描出されることを認めた（図3C, D）。さらに、^{99m}Tc標識抗LOX-1抗体は、現在動脈硬化プラークの核医学診断用放射性薬剤として有力視されている^{99m}Tc標識annexin A5と比較して、動脈硬化病変への放射能集積、および、比較的安定な病変に対する放射能集積比の両者において高い値を示した（図3E）[6]。以上の結果より、不安定プラークイメージング剤として^{99m}Tc標識抗LOX-1抗体の開発に成功した。さらに、この成果を基盤に不安定プラークのPETイメージング剤として^{64}Cu、^{68}Ga標識抗LOX-1抗体の開発を検討中である。

4. おわりに

癌（悪性新生物）に次ぐ日本人の死因は心疾患・脳血管疾患であり、この二つを合わせると癌に匹敵する数となる。したがって、これらの引き金となる不安定プラークの質的診断法の開発が切望され、様々な分子プローブが開発されつつある。本稿では浸潤マクロファージのエネルギー活動を集積機序とする^{18}F-FDG、プラークの不安定性と関連するLOX-1を標的とする^{99m}Tc標識抗LOX-1抗体に関する研究を紹介した。今後さらに、^{18}F-FDG、^{99m}Tc標識抗LOX-1抗体に加えて、破綻を起こす危険性の高い不安定プラークを特異的に検出することのできる分子プローブが開発されれば、^{18}F-FDG、^{99m}Tc標識抗LOX-1抗体と組み合わせることで、動脈硬化疾患の病態進行の把握が可能となり、効果的・効率的なテーラーメイド医療の推進が期待される。

参考文献

1) Choudhury R. P., Fuster V. and Fayad Z. A., *Nat Rev Drug Discov*, **3**, 913-25, (2004)
2) Ogawa M., Ishino S., Mukai T., Asano D., Teramoto N., Watabe H., Kudomi N., Shiomi M., Magata Y., Iida H. and Saji H., *J Nucl Med*, **45**, 1245-50, (2004)
3) Ogawa M., Magata Y., Kato T., Hatano K., Ishino S., Mukai T., Shiomi M., Ito K. and Saji H., *J Nucl Med*, **47**, 1845-50, (2006)
4) Ishino S., Mukai T., Kume N., Asano D., Ogawa M., Kuge Y., Minami M., Kita T., Shiomi M. and Saji H., *Atherosclerosis*, **195**, 48-56, (2007)
5) Ishino S., Mukai T., Kuge Y., Kume N., Ogawa M., Takai N., Kamihashi J., Shiomi M., Minami M., Kita T. and Saji H., *J Nucl Med*, **49**, 1677-85, (2008)
6) Ishino S., Kuge Y., Takai N., Tamaki N., Strauss H. W., Blankenberg F. G., Shiomi M. and Saji H., *Eur J Nucl Med Mol Imaging*, **34**, 889-99, (2007)
7) Libby P., Geng Y. J., Aikawa M., Schoenbeck U., Mach F., Clinton S. K., Sukhova G. K. and Lee R. T., *Curr Opin Lipidol*, **7**, 330-5, (1996)
8) Zhou J., Chew M., Ravn H. B. and Falk E., *Scand J Clin Lab Invest Suppl*, **230**, 3-11, (1999)
9) Libby P., *Am J Cardiol*, **86**, 3J-8J; discussion 8J-9J, (2000)
10) Virmani R., Burke A. P., Farb A. and Kolodgie F. D., *Prog Cardiovasc Dis*, **44**, 349-56, (2002)
11) Kuge Y., Kume N., Ishino S., Takai N., Ogawa Y., Mukai T., Minami M., Shiomi M. and Saji H., *Biol Pharm Bull*, **31**, 1475-82, (2008)

Development of a Radiolabeled Probe for Detecting Membrane Type-1 Matrix Metalloproteinase on Malignant Tumors

Takashi TEMMA,[a] Kohei SANO,[a] Yuji KUGE,*[,a,b] Junko KAMIHASHI,[a] Nozomi TAKAI,[a] Yuki OGAWA,[a] and Hideo SAJI[a]

[a] *Department of Patho-Functional Bioanalysis, Graduate School of Pharmaceutical Sciences, Kyoto University; 46–29 Yoshida Shimoadachi-cho, Sakyo-ku, Kyoto 606–8501, Japan: and* [b] *Department of Tracer Kinetics & Bioanalysis, Graduate School of Medicine, Hokkaido University; Kita 15 Nishi 7, Kita-ku, Sapporo 060–8638, Japan.*

Received February 3, 2009; accepted May 7, 2009; published online May 8, 2009

Membrane type-1 matrix metalloproteinase (MT1-MMP) expressed on the tumor cell surface activates pro-MMP-2 and pro-MMP-13 to exacerbate the malignancy, suggesting its suitability as a target molecule for diagnosis by *in vivo* molecular imaging. Thus, we prepared radiolabeled anti-MT1-MMP monoclonal antibody (mAb) as a novel radiolabeled probe for detecting MT1-MMP *in vivo* and evaluated its usefulness in breast tumor-bearing rodents. ^{99m}Tc-anti-MT1-MMP mAb was prepared using HYNIC as a bifunctional chelating agent and immunoreactivity was evaluated by flow cytometry. MT1-MMP expression in breast carcinoma cells (rat: Walker-256 and MRMT-1, mouse: FM3A) was measured by Western blotting. *In vivo* biodistribution was examined for 48 h using tumor-implanted rodents followed by estimation of radiation absorbed by a standard quantitation platform Organ Level Internal Dose Assessment (OLINDA). ^{99m}Tc-anti-MT1-MMP mAb was obtained with 84% immunoreactivity to MT1-MMP and more than 92% radiochemical purity. MT1-MMP was highly expressed in all malignant cells. Tumor radioactivity increased with time after administration and reached 3 to 5 times higher values at 24 h post-injection than those at 1 h. Other organs, including the stomach, showed decreasing values over time. Tumor to blood ratios increased with time and reached more than 1.3 at 48 h. The effective dose was <5.0 μSv/MBq. The results suggest that ^{99m}Tc-anti-MT1-MMP mAb is a promising probe for future diagnosis of breast tumors by *in vivo* nuclear medical imaging.

Key words membrane type-1 matrix metalloproteinase; breast tumor; non-invasive imaging; single photon emission computed tomography

Effective methods for detecting malignant tumors in the early phase before any obvious progression has occurred permits optimal conditions for successful therapy.[1,2] Nuclear medical techniques such as single photon emission computed tomography (SPECT) and positron emission tomography (PET) are non-invasive and have the potential to provide sensitive diagnoses. Both techniques detect radiation emitted from a radiolabeled probe targeted to a biological molecule relevant to tumor malignancy.

Matrix metalloproteinases (MMPs) play important roles in tumor growth, invasion and metastasis by degrading extracellular matrix components.[3] MMPs are classified as secreted MMPs or membrane-associated MMPs (MT-MMPs) based on their structure.[4] Among MT-MMPs, MT1-MMP activates pro-MMP-2 and pro-MMP-13 on the cell surface especially at lamellipodia, the migration front of cells.[5] Therefore, MT1-MMP has a close relationship with tumor malignancy.[6,7] As a target molecule of a radiolabeled probe, it is important to be localized at the site of malignancy in order to obtain clear images that can be readily compared or fused to anatomical information. In cases where target molecules are secreted to the surrounding tissues or bodily fluids including blood, a fall of signal to noise ratio in images is inevitable. MT1-MMP is a good candidate target as expression of MT1-MMP remains localized in tumor tissues[4] and increases in the early phase of exacerbation.[8] Further, since the amino acid sequences of MT1-MMP protein are well preserved among species including mouse, rat, rabbit and human,[9] results obtained in experiments using rodents and MT1-MMP probes may provide important information for clinical applications. Thus, MT1-MMP is a potential target for imaging and diagnosing malignant tumors at early phases. Among all types of tumors, breast cancer remains a predominant cause of death from cancer in women despite advances in the treatment, especially in cases where distant metastases occur.[10] This motivated us to select breast cancer as a target disease for investigation of the MT1-MMP probe.

To the best of our knowledge, there have been no reports on the development of an MT1-MMP imaging agent for *in vivo* nuclear medical imaging. Therefore, in this study, we prepared Tc-99m-labeled anti-MT1-MMP monoclonal antibody and evaluated its usefulness through biodistribution studies using three kinds of rodent models bearing breast tumor allografts.

MATERIALS AND METHODS

Preparation of ^{99m}Tc-Anti-MT1-MMP mAb All chemicals used in this study were commercial products of the highest purity. ^{99m}Tc-pertechnetate was eluted in saline solution on a daily basis from ^{99}Mo-^{99m}Tc generators (Ultra-Techne Kow®, FUJIFILM RI Pharma Co., Ltd., Tokyo, Japan). Succinimidyl hydrazinopyridine-3-carboxylate (HYNIC-NHS) was synthesized following the procedure reported previously.[11] Anti-MT1-MMP mAb (113-5B7, Daiichi Fine Chemical Co., Ltd., Toyama, Japan), a purified mouse monoclonal antibody to an oligopeptide (residues 319 to 333, numbered from the signal peptide) of human MT1-MMP, was used for experiments after further purification on a HiTrap rProtein A column (17-5080-01, GE Healthcare, U.K.). HYNIC-NHS (25 μl, 5 mg/ml) in dry *N,N*-dimethylformamide (DMF) was added to anti-MT1-MMP mAb solu-

* To whom correspondence should be addressed. e-mail: kuge@med.hokudai.ac.jp

tion in 0.15 M borate buffer (pH 8.5, 2 mg/400 μl). After gentle stirring with protection from light for 2 h at room temperature, size-exclusion filtration with a diafiltration membrane (Amicon Ultra 4 (MWCO 30000), Millipore Co., Billerica, MA, U.S.A.) using 0.01 M citrate buffer (pH 5.2) was performed to obtain HYNIC-anti-MT1-MMP mAb. The protein concentration of the purified solution was determined by the bicinchoninate (BCA) method.[12]

An equal volume of ^{99m}Tc-(tricine)$_2$ (530±18 MBq), prepared by the method of Larsen *et al.*,[13] was added to a solution of HYNIC-anti-MT1-MMP mAb (1 ml, 1 mg/ml) in 0.01 M citrate buffer (pH 5.2). After 3 h at room temperature, size-exclusion filtration with a PD-10 column using 0.05 M phosphate buffered saline (PBS) (pH 7.0) was performed to obtain the ^{99m}Tc-anti-MT1-MMP mAb. Radiochemical purity of ^{99m}Tc-anti-MT1-MMP mAb, evaluated by another size-exclusion filtration (PD-10 column), was more than 92%. Radiochemical yield was 29.9±7.5%. Mouse immunoglobulin G_3 (IgG_3), kappa mAb (ab18392, Abcam, Cambridge, U.K.) was radiolabeled in a similar way as a negative control for biodistribution studies.

Immunoreactivity of HYNIC-Anti-MT1-MMP mAb Antibodies (50 μg/ml, 100 μl; anti-MT1-MMP mAb, HYNIC-anti-MT1-MMP mAb or negative control IgG_3 (sc-3880, Santa Cruz Biotechnology, California, U.S.A.)) were added to mouse macrophage cells (RAW264.7, 2×10^6 cells) and incubated in 0.01 M PBS (pH 7.4, 100 μl) for 30 min on ice. After washing with 0.01 M PBS, Alexa Fluor® 488 goat anti-mouse IgG antibody (A-11001, Molecular Probes, Eugene, OR, U.S.A.) (10 μg/ml, 100 μl) was added for 30 min on ice. Fluorescence levels were measured using a flow cytometer (Becton Dickinson Inc., Franklin Lakes, NJ, U.S.A.). Data were analyzed using BD CellQuest Pro (BD Biosciences, San Jose, CA, U.S.A.) and a figure was calculated by the following equation: median fluorescence intensity of anti-MT1-MMP mAb or HYNIC-anti-MT1-MMP mAb divided by the median fluorescence intensity of negative control IgG. This was used as an index of immunoreactivity of anti-MT1-MMP mAb and HYNIC-anti-MT1-MMP mAb.

***In Vitro* Stability of ^{99m}Tc-Anti-MT1-MMP mAb in Rodent Plasma** ^{99m}Tc-Anti-MT1-MMP mAb (30 μl) was added to rat (n=4) or mouse (n=3) plasma (270 μl) collected from female Sprague-Dawley (SD) rats or female C3H/He mice. Plasma samples were incubated at 37 °C for 48 h. After incubation, 50 to 100 μl aliquots of samples were drawn and radioactivity was analyzed by size-exclusion chromatography with a PD-10 column using 0.05 M PBS (pH 7.0).

Preparation of Tumor-Bearing Animals Female SD rats (8 weeks old) and female C3H/He mice (5 weeks old), supplied by Japan SLC, Inc. (Hamamatsu, Japan), were housed under a 12-h light/12-h dark cycle and given free access to food and water. The animal experiments in this study were conducted in accordance with institutional guidelines and approved by the Kyoto University Animal Care Committee, Japan.

Rat breast carcinoma cells (Walker-256 and MRMT-1) and mouse breast carcinoma cells (FM3A) were supplied by the Cell Resource Center for Biomedical Research, Tohoku University and Health Science Research Resources Bank (HSRRB) (Osaka, Japan). Cells were cultured in RPMI1640 medium supplemented with 10% fetal bovine serum at 37 °C in a humidified atmosphere containing 5% CO_2 and 95% air.

Walker-256 and MRMT-1 cells were suspended in 0.01 M PBS (pH 7.4) followed by subcutaneous inoculation into the right hind flank of rats (10^6 cells/100 μl PBS/rat). FM3A cells were suspended in PBS followed by subcutaneous inoculation into the right hind leg of mice (5×10^6 cells/100 μl PBS/mouse). Tumor volume was estimated by [(length)×(width)^2]/2[14] over a 10- to 14-d tumor growth period. The average size of the tumors was 860±960 mm^3, 790±280 mm^3 and 230±170 mm^3 for Walker-256, MRMT-1 and FM3A, respectively, on the day before the biodistribution studies.

Western Blotting Cell lysates were prepared from Walker-256, MRMT-1 and FM3A cells by homogenization in passive lysis buffer (E194A, Promega, WI, U.S.A.) containing protease inhibitor (P8340, Sigma Aldrich Co., MO, U.S.A.). Protein content of the lysates was determined by the BCA method and 5.0 μg of protein/lane was subjected to electrophoresis on 5—20% sodium dodecyl sulfate (SDS)-polyacrylamide gels followed by transfer to polyvinylidene difluoride membranes. After blocking with Blocking One (03953-95, Nacalai Tesque, Inc., Kyoto, Japan), membranes were incubated with anti-MT1-MMP antibody followed by horseradish peroxidase-conjugated goat anti-mouse IgG_3 antibody. Bands were visualized by ECL plus Western Blotting Detection System (RPN2132, GE Healthcare, U.K.) with a Luminocapture instrument (BIO-RAD Laboratories, Osaka, Japan). Immunoblotting for β-actin was used as a protein loading control.

***In Vivo* Biodistribution Study** Animals were divided into 5 groups (n=3—4 each) for 5 time points with approximately equal distribution of tumor sizes on the day before the study. Animals were fasted for 6 h before administration of radiopharmaceutical. At 1, 3, 6, 24, and 48 h after intravenous administration of ^{99m}Tc-anti-MT1-MMP mAb (3.4±0.9 MBq, 50 μg/200 μl PBS for rats, 50 μg/100 μl PBS for mice), animals were euthanized. The blood, heart, lung, liver, kidney, stomach, intestine, spleen, pancreas, brain, muscle and tumor were excised, weighed and counted for radioactivity with a NaI well-type scintillation counter (1470 WIZARD, PerkinElmer Japan Co., Osaka, Japan). In addition, biodistribution of ^{99m}Tc-negative control mAb was evaluated in MRMT-1 implanted rats in a similar way.

Radiation Absorbed Dose For estimating radiation absorbed doses, source organ residence times were determined by calculating the area under non-decay-corrected time–activity curves generated for each organ using averaged biodistribution data. Projected radiation absorbed doses for humans were made by assuming that the metabolism rates and pharmacokinetics of ^{99m}Tc-anti-MT1-MMP mAb in humans and rodents are equivalent, as previously reported.[15] Absorbed doses and effective dose were estimated with a standard quantitation platform Organ Level Internal Dose Assessment (OLINDA; Vanderbilt University).[16]

RESULTS

***In Vitro* Studies** Indices of immunoreactivity evaluated by flow cytometry analyses were 5.83±3.05 and 6.13±2.73 for the HYNIC-anti-MT1-MMP mAb and anti-MT1-MMP mAb, respectively. This showed that the HYNIC-anti-MT1-

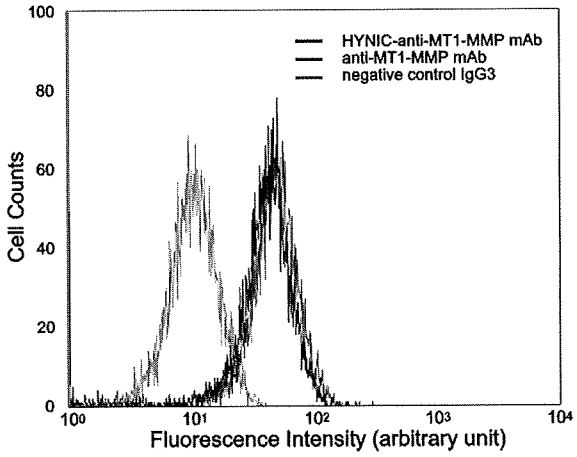

Fig. 1. A Representative FACS Overlay Histogram of Binding of Anti-MT1-MMP mAb, HYNIC-Anti-MT1-MMP mAb and Negative Control IgG_3 to Mouse Macrophages (RAW 264.7)

Immunoreactivities of anti-MT1-MMP mAb and HYNIC-anti-MT1-MMP mAb were evaluated with the median fluorescence intensity ratio compared to negative control mouse IgG_3.

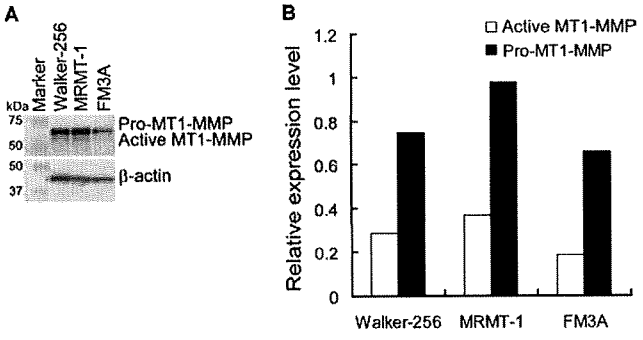

Fig. 2. (A) Western Blot Analyses of MT1-MMP (Pro- and Active-Forms) and β-Actin Expression in Walker-256, MRMT-1 and FM3A Cells and (B) Densitometry Analyses of the Bands in (A)

The levels of pro- and active-MT1-MMP were normalized to the level of β-actin protein.

MMP mAb retained 93% immunoreactivity of the anti-MT1-MMP mAb (Fig. 1). Forty-eight hours after initiation of incubation in rat and mouse plasmas at 37 °C, more than 92% of ^{99m}Tc-anti-MT1-MMP mAb remained in an unchanged form.

Western Blotting Cell lysates were subjected to Western blot analysis to examine the quantities of MT1-MMP (Fig. 2). Expression of both the pro- (63 kDa) and active- (58 kDa) forms of MT1-MMP protein was detected in Walker-256, MRMT-1 and FM3A cells. When normalized to the level of β-actin protein, as represented in Fig. 2B, similar expression levels were confirmed.

***In Vivo* Biodistribution Studies** Results of *in vivo* biodistribution studies are summarized in Table 1 (Walker-256 and MRMT-1) and Table 2 (FM3A). In tumors, radioactivity increased in a time-dependent manner and at 24 h post-injection, 3 to 5 times higher accumulations were achieved than those at 1 h. Values in % dose/g at 1 and 24 h post-injection were 0.41±0.15 and 2.04±0.65 in Walker-256, 0.44±0.12 and 1.42±0.08 in MRMT-1, and 2.63±0.59 and 15.00±0.48 in FM3A, respectively. Radioactivity in the kidneys was rather high among organs in all three tumor animal models. Values in % dose/g in the kidneys were 3.23±0.21

Table 1. Biodistribution of Radioactivity after Injection of ^{99m}Tc-Anti-MT1-MMP mAb in SD Rats Bearing Walker-256 or MRMT-1 Rat Breast Tumors[a)]

Tissue	Time after injection				
	1 h	3 h	6 h	24 h	48 h
			Walker-256		
Blood	5.28 (0.52)	4.75 (0.52)	4.43 (0.77)	2.07 (0.43)	1.22 (0.15)
Heart	0.75 (0.08)	0.84 (0.11)	0.86 (0.08)	0.60 (0.16)	0.44 (0.05)
Lung	2.51 (0.27)	1.48 (0.13)	1.90 (0.33)	1.16 (0.24)	1.22 (0.73)
Liver	1.89 (0.28)	2.28 (0.15)	2.59 (0.19)	2.09 (0.32)	2.05 (0.26)
Kidney	1.67 (0.10)	2.00 (0.19)	2.12 (1.18)	2.84 (0.48)	3.23 (0.21)
Intestine	0.25 (0.03)	0.46 (0.07)	0.57 (0.11)	0.45 (0.15)	0.28 (0.03)
Pancreas	0.41 (0.10)	0.35 (0.17)	0.31 (0.10)	0.52 (0.29)	0.45 (0.08)
Spleen	1.60 (0.06)	1.66 (0.15)	1.80 (0.30)	1.86 (0.28)	1.68 (0.31)
Muscle	0.07 (0.01)	0.07 (0.02)	0.07 (0.02)	0.11 (0.05)	0.11 (0.06)
Brain	0.11 (0.01)	0.10 (0.02)	0.10 (0.02)	0.06 (0.01)	0.03 (0.00)
Tumor	0.41 (0.15)	0.71 (0.13)	1.09 (0.31)	2.04 (0.65)	1.76 (0.31)
Stomach[b)]	0.86 (0.10)	1.18 (0.10)	1.20 (0.41)	0.72 (0.29)	0.38 (0.11)
Urine[b)]				17.62 (1.00)	24.97 (1.05)
Feces[b)]				5.29 (1.74)	8.94 (2.11)
Tumor/blood	0.08 (0.03)	0.15 (0.04)	0.24 (0.06)	0.97 (0.17)	1.46 (0.26)
Tumor/muscle	5.79 (1.99)	10.67 (1.37)	16.69 (3.20)	21.20 (5.48)	19.99 (10.66)
			MRMT-1		
Blood	4.90 (0.42)	3.94 (0.21)	3.77 (0.30)	1.66 (0.16)	0.94 (0.09)
Heart	0.88 (0.06)	0.85 (0.19)	0.88 (0.14)	0.55 (0.06)	0.36 (0.06)
Lung	1.51 (0.11)	1.72 (0.47)	1.56 (0.28)	1.08 (0.11)	0.71 (0.03)
Liver	1.43 (0.13)	1.50 (0.09)	1.71 (0.14)	1.13 (0.15)	1.21 (0.18)
Kidney	1.75 (0.11)	2.14 (0.29)	2.73 (0.06)	2.93 (0.15)	3.05 (0.29)
Intestine	0.26 (0.03)	0.39 (0.06)	0.61 (0.08)	0.26 (0.01)	0.20 (0.03)
Pancreas	0.30 (0.05)	0.22 (0.04)	0.30 (0.10)	0.32 (0.01)	0.21 (0.03)
Spleen	1.14 (0.18)	1.06 (0.11)	1.17 (0.04)	0.97 (0.12)	0.92 (0.08)
Muscle	0.08 (0.01)	0.06 (0.01)	0.05 (0.02)	0.09 (0.01)	0.07 (0.06)
Brain	0.12 (0.02)	0.08 (0.00)	0.08 (0.00)	0.04 (0.01)	0.03 (0.00)
Tumor	0.44 (0.12)	0.73 (0.11)	1.01 (0.19)	1.42 (0.08)	1.20 (0.15)
Stomach[b)]	0.36 (0.03)	0.43 (0.03)	0.69 (0.41)	0.52 (0.06)	0.25 (0.02)
Urine[b)]				12.08 (0.33)	16.76 (1.03)
Feces[b)]				2.40 (1.14)	4.71 (0.79)
Tumor/blood	0.09 (0.02)	0.18 (0.03)	0.27 (0.06)	0.86 (0.07)	1.28 (0.18)
Tumor/muscle	5.85 (1.95)	12.49 (2.76)	20.75 (6.51)	16.74 (1.50)	16.79 (7.67)

a) Tissue radioactivity is expressed as % injected dose per gram. Each value represents the mean (±S.D.) for four animals at each interval. *b*) Expressed as % injected dose.

Table 2. Biodistribution of Radioactivity after Injection of ^{99m}Tc-Anti-MT1-MMP mAb in C3H/He Mice Bearing FM3A Mouse Breast Tumors[a)]

Tissue	Time after injection				
	1 h	3 h	6 h	24 h	48 h
Blood	37.05	31.68	29.78	14.43	11.00
	(2.09)	(4.75)	(4.19)	(0.83)	(0.10)
Heart	6.69	6.54	6.89	4.93	4.45
	(0.61)	(2.39)	(0.89)	(0.29)	(0.47)
Lung	20.21	16.72	13.59	7.92	6.25
	(4.11)	(0.58)	(1.55)	(1.32)	(0.60)
Liver	8.46	9.03	8.02	5.76	5.33
	(1.39)	(0.84)	(0.70)	(0.42)	(0.40)
Kidney	9.01	10.75	10.63	8.20	8.80
	(1.55)	(1.23)	(1.60)	(0.27)	(0.27)
Intestine	2.47	4.47	7.09	2.47	2.20
	(0.49)	(0.80)	(0.94)	(0.32)	(0.30)
Pancreas	1.00	1.49	1.60	1.77	2.08
	(0.15)	(0.13)	(0.51)	(0.15)	(0.22)
Spleen	7.27	7.09	6.10	5.66	6.57
	(1.04)	(1.04)	(0.90)	(0.20)	(0.78)
Muscle	0.48	0.62	0.64	1.28	1.88
	(0.05)	(0.04)	(0.29)	(0.39)	(0.39)
Brain	0.63	0.49	0.44	0.28	0.33
	(0.21)	(0.10)	(0.06)	(0.02)	(0.01)
Tumor	2.63	4.10	5.97	15.00	16.99
	(0.59)	(1.44)	(1.64)	(0.48)	(1.81)
Stomach[b)]	0.28	0.41	0.55	0.49	0.54
	(0.04)	(0.09)	(0.17)	(0.02)	(0.10)
Urine[b,c)]				4.94	14.85
Feces[b,c)]				1.17	3.85
Tumor/blood	0.07	0.13	0.21	1.04	1.54
	(0.02)	(0.04)	(0.07)	(0.06)	(0.17)
Tumor/muscle	5.42	6.58	9.83	12.37	9.39
	(0.73)	(2.24)	(1.63)	(2.93)	(2.33)

a) Tissue radioactivity is expressed as % injected dose per gram. Each value represents the mean (±S.D.) for three (1 h) and four (3, 6, 24, 48 h) animals. *b*) Expressed as % injected dose. *c*) Calculated using summated radioactivity of four animals.

in Walker-256, 3.05±0.29 in MRMT-1 and 8.80±0.27 in FM3A, respectively, at 48 h post-injection. Other tissues, including the stomach, showed decreasing or constant radioactivity levels over time. Values in % dose in the stomach at 48 h post-injection were 0.38±0.11 in Walker-256, 0.25±0.02 in MRMT-1 and 0.54±0.10 in FM3A.

Tumor to blood (T/B) and tumor to muscle (T/M) ratios were calculated as indicators of availability of ^{99m}Tc-anti-MT1-MMP mAb for *in vivo* imaging. T/B ratios increased in a similar manner as the radioactivity in tumors. Ratios obtained were 1.46±0.26 in Walker-256, 1.28±0.18 in MRMT-1 and 1.54±0.17 in FM3A at 48 h post-injection. T/M ratios exhibited constantly high values after 6 h post-injection (16.69±3.20 in Walker-256, 20.75±6.51 in MRMT-1 and 9.83±1.63 in FM3A). T/B ratios of ^{99m}Tc-negative control mAb in MRMT-1 are also shown in Fig. 3. The values were 0.66±0.05 at 24 h and 0.81±0.09 at 48 h post-injection. The time-course of ^{99m}Tc-anti-MT1-MMP mAb was significantly higher than that of the ^{99m}Tc-negative control mAb by two factor factorial ANOVA assay ($p<0.0001$).

Radiation Absorbed Dose Radiation absorbed doses (μSv/MBq) were estimated using data of biodistribution studies with ^{99m}Tc-anti-MT1-MMP mAb (Table 3). The highest radiation dose was to the kidneys, followed by the liver, the intestine and the spleen. The effective dose was 4.4 to 5.0 μSv/MBq.

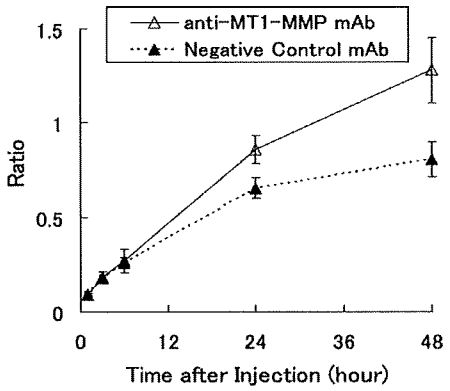

Fig. 3. Tumor to Blood (T/B) Ratios of Radioactivity after Administration of ^{99m}Tc-Anti-MT1-MMP mAb (Open Triangle) or ^{99m}Tc-Negative Control mAb (Close Triangle) to Rats Bearing MRMT-1 Breast Tumors

Error bars represent standard deviations. Two factor factorial ANOVA analyses determined significant difference between the time-courses of ^{99m}Tc-anti-MT1-MMP mAb and ^{99m}Tc-negative control mAb ($p<0.0001$).

Table 3. Radiation Dose (μSv/MBq) Estimated for ^{99m}Tc-Anti-MT1-MMP mAb

	Walker-256	MRMT-1	FM3A
Heart	5.7	6.0	6.3
Lung	5.8	5.1	7.2
Liver	23.8	16.8	12.4
Kidney	20.6	21.8	15.6
Intestine	11.5	12.3	12.5
Pancreas	6.9	6.1	6.0
Spleen	10.7	8.7	7.9
Muscle	1.5	1.8	2.2
Brain	0.5	0.8	1.2
Stomach	6.9	5.4	5.4
Red marrow	1.9	2.5	3.0
Osteogenic cells	3.3	5.4	7.1
Ovaries	3.2	4.2	4.9
Uterus	2.9	3.9	4.6
Total body	2.5	3.0	3.4
Effective dose	4.4	4.7	5.0
Effective dose equivalent	6.5	6.4	6.4

DISCUSSION

We prepared ^{99m}Tc-anti-MT1-MMP mAb with a sustained immunoreactivity comparable to anti-MT1-MMP mAb and high radiochemical purity, and evaluated its usefulness through biodistribution studies using breast tumor-implanted rodents. The effectiveness of ^{99m}Tc-anti-MT1-MMP mAb for detecting breast tumors expressing MT1-MMP, that is 'malignant tumors', was demonstrated since radioactivity in tumors and T/B and T/M ratios increased with time after administration of ^{99m}Tc-anti-MT1-MMP mAb in all three tumor models. T/B ratios of ^{99m}Tc-anti-MT1-MMP mAb were significantly higher than those of the ^{99m}Tc-negative control mAb, indicating the specificity of ^{99m}Tc-anti-MT1-MMP mAb toward MT1-MMP. The moderate accumulation of ^{99m}Tc-negative control mAb in tumors could be due to the enhanced permeability and retention (EPR) effect, which is characterized by enhanced permeability of tumor vasculatures and little lymphatic recovery.[17] Importantly, other tissues including the stomach showed a concomitant decrease

in radioactivity over time. In addition, the biodistribution results exhibiting high accumulation in tumors also indicated the suitability of this antibody for radioimmunotherapy. Together, this suggests that the radiolabeled antibody is a promising probe for *in vivo* nuclear medical imaging, such as single photon emission computed tomography (SPECT), for future diagnoses of breast tumors. Although further investigations are needed for more sensitive detection, it should be emphasized that this is the first report of development of an *in vivo* probe targeted to MT1-MMP. Also, the development of such an imaging agent provides a strong tool for clarification of the roles of MT1-MMP on tumors *in vivo*, which may lead to development of a novel pharmaceutical.

In the present study, technetium-99m was used to label anti-MT1-MMP mAb because of its optimal characteristics for *in vivo* imaging in clinical settings. This then led to the selection of HYNIC as a bifunctional chelating agent since it has high stability by coordination with Tc-99m and two molecules of tricine.[11] As expected, ^{99m}Tc-anti-MT1-MMP mAb was stable in plasma. Furthermore, the low radioactivity detected in the stomach indicated the *in vivo* stability of ^{99m}Tc-anti-MT1-MMP mAb against dissociation of Tc-99m from HYNIC and oxygenation to ^{99m}Tc pertechnetate. If dissociation had occurred, ^{99m}Tc pertechnetate would have been taken up by the epithelial cells that line the mucosal surface of the stomach *via* the sodium iodide symporter system[18,19] and the radioactivity detected would have been much higher. The high stability of the radioligand was essential for further evaluation.

Relatively slow washout of radioactivity from the blood might be a drawback for the imaging ability of ^{99m}Tc-anti-MT1-MMP mAb. Previous researchers reported that this could be overcome by fragmentation of the antibody or synthesis of small-molecule derivatives.[20,21] In addition, moderate radioactivities in the kidneys, liver and spleen were observed in biodistribution studies that were not due to MT1-MMP expression.[4] However, these radioactivities might not affect the imaging quality of breast tumors. To estimate the effective dose of the ^{99m}Tc-anti-MT1-MMP mAb, which is an estimate of the stochastic effect that a non-uniform radiation dose has on a human, the OLINDA estimation gave a maximum value of 5.0 μSv/MBq. This value is similar to the average effective dose in nuclear medicine,[22] indicating that the use of ^{99m}Tc-anti-MT1-MMP mAb may be acceptable for *in vivo* imaging in humans.

Several MMP imaging probes have been developed for detecting states of MMP-dependent diseases such as cancer, atherosclerosis, stroke, and other pathophysiologies. Among them, radiolabeled broad-spectrum MMP inhibitors (MPIs) have been mostly investigated during *in vitro* and *in vivo* evaluations.[23,24] Some of these radiolabeled MPIs exhibited promising pharmacodynamics partly due to their low molecular weight. However, these small molecular probes mainly recognize soluble MMPs including MMP-2, -3, -9, and -13, while our ^{99m}Tc-anti-MT1-MMP mAb recognizes a membrane-bound MMP, MT1-MMP. As a target molecule of a radiolabeled probe, it is important to be localized at the site of malignancy in order to obtain clear images that can be readily compared to anatomical information. Background levels can become elevated in cases where target molecules are secreted to the surrounding tissues or bodily fluids including blood. Therefore, it may be advantageous to utilize MT1-MMP rather than soluble MMPs as a target molecule for detecting cancer malignancy. In addition, the use of a monoclonal antibody and/or an antibody derivative as a fundamental part of radiolabeled probe is significantly superior to radiolabeled MPIs for strict targeting to a specific MMP.

In this study, three breast tumor cell lines, MRMT-1, Walker 256 and FM3A, from two different species were used in order to evaluate the prevalence of the radiolabeled probe. MRMT-1 is a rat mammary gland carcinoma cell line generally used for studies of bone pain,[25] where bones inoculated with these cells showed infiltration of bone marrow spaces by malignant tumors.[26] Walker 256 is also a rat breast carcinoma cell line used in a variety of cancer studies. As previously reported in a histological study,[27] these cells show several ultrastructural features that typically designate malignancy. FM3A is a murine mammary carcinoma cell line especially used in studies on hypoxia in tumors,[28] where cells showed high radioresistance.[29] Therefore, all these cell lines give rise to malignant tumors and, as expected, the expression of MT1-MMP protein was comparable in each. Similar accumulations of radioactivity in tumors were found in the biodistribution experiments.

It is known that MT1-MMP is subject to recycling.[30] MT1-MMP is produced inside the cell by cleavage of the pro-domain of pro-MT1-MMP by furin, transited to the cell membrane, dimerized, followed by complex formation with TIMP-2 to activate pro-MMP2, and finally internalized into the cell. Dimerization of MT1-MMPs occurs by interaction of the hemopexin-like domains, a region between the transmembrane domain and catalytic domain, of two separate molecules of MT1-MMP.[31] The epitope of the antibody used in this study was in the hemopexin-like domain so that reactions between the antibody and MT1-MMP, and between two molecules of MT1-MMP, could potentially compete for each other on the cell surface. Although it was not elucidated whether this competition would affect the results, providing that it does occur *in vivo* like pertuzumab,[32] imaging efficiency may be further improved using an alternative antibody whose epitope is in a different domain of MT1-MMP.

The amino acid sequences of MT1-MMP protein are well preserved among species, including mouse, rat, rabbit and human.[9] The antibody used here was an anti-human MT1-MMP mouse monoclonal antibody IgG_3, though results were obtained in a rodent animal model in this study. In addition, this antibody is suited for detection of human MT1-MMP by preliminary Western blot analysis using lysates from human breast cancer cells (MDA-MB-231) (data not shown). Thus, the preferable outcomes reported for rodents might be easily translated to a clinical situation, after the antibody is optimally humanized to lose immunogenicity and endure metabolism in the body.

MT1-MMP is reported to experience shedding by other proteases on the cell surface leading to soluble MT1-MMP secreted into the blood.[33] Although a variety of forms of soluble MT1-MMP have been reported due to differences in the position of cleavage,[34] it is unclear whether the antibody used in this study would react with soluble MT1-MMP in the blood. Since the biodistribution experiments of ^{99m}Tc-anti-MT1-MMP mAb showed a normal, or rather fast, clearance from the body, soluble MT1-MMP in the blood might not af-

fect the results.

CONCLUSION

^{99m}Tc-anti-MT1-MMP mAb accumulated in malignant tumors of all three animal models with a low effective dose, while radioactivity disappeared in non-targeted organs. The results suggest that the ^{99m}Tc-anti-MT1-MMP mAb is a promising probe for *in vivo* nuclear medical imaging for future diagnosis of breast tumors.

Acknowledgments This study was supported by Grants-in-Aid for Scientific Research and by the 21st Century Center of Excellence Programs at Kyoto University "Knowledge Information Infrastructure for Genome Science" from the Ministry of Education, Culture, Sports, Science and Technology of Japan. Part of this study was conducted as part of the project, "R&D of Molecular Imaging Equipment for Malignant Tumor Therapy Support," supported by the New Energy and Industrial Technology Development Organization (NEDO) of Japan.

REFERENCES

1) DeNardo S. J., *Semin. Nucl. Med.*, **35**, 143—151 (2005).
2) Slamon D. J., Leyland-Jones B., Shak S., Fuchs H., Paton V., Bajamonde A., Fleming T., Eiermann W., Wolter J., Pegram M., Baselga J., Norton L., *N. Engl. J. Med.*, **344**, 783—792 (2001).
3) Deryugina E. I., Quigley J. P., *Cancer Metastasis Rev.*, **25**, 9—34 (2006).
4) Sato H., Takino T., Okada Y., Cao J., Shinagawa A., Yamamoto E., Seiki M., *Nature* (London), **370**, 61—65 (1994).
5) Mori H., Tomari T., Koshikawa N., Kajita M., Itoh Y., Sato H., Tojo H., Yana I., Seiki M., *EMBO J.*, **21**, 3949—3959 (2002).
6) Jones J. L., Glynn P., Walker R. A., *J. Pathol.*, **189**, 161—168 (1999).
7) Knauper V., Bailey L., Worley J. R., Soloway P., Patterson M. L., Murphy G., *FEBS Lett.*, **532**, 127—130 (2002).
8) Chen P. S., Zhai W. R., Zhou X. M., Zhang J. S., Zhang Y. E., Ling Y. Q., Gu Y. H., *World J. Gastroenterol.*, **7**, 647—651 (2001).
9) Sato T., del Carmen Ovejero M., Hou P., Heegaard A. M., Kumegawa M., Foged N. T., Delaisse J. M., *J. Cell Sci.*, **110**, 589—596 (1997).
10) Jemal A., Murray T., Ward E., Samuels A., Tiwari R. C., Ghafoor A., Feuer E. J., Thun M. J., *CA Cancer J. Clin.*, **55**, 10—30 (2005).
11) Abrams M. J., Juweid M., tenKate C. I., Schwartz D. A., Hauser M. M., Gaul F. E., Fuccello A. J., Rubin R. H., Strauss H. W., Fischman A. J., *J. Nucl. Med.*, **31**, 2022—2028 (1990).
12) Smith P. K., Krohn R. I., Hermanson G. T., Mallia A. K., Gartner F. H., Provenzano M. D., Fujimoto E. K., Goeke N. M., Olson B. J., Klenk D. C., *Anal. Biochem.*, **150**, 76—85 (1985).
13) Larsen S. K., Solomon H. F., Caldwell G., Abrams M. J., *Bioconjug. Chem.*, **6**, 635—638 (1995).
14) Zhang Y., Wang C., Sun M., *Biochem. Biophys. Res. Commun.*, **325**, 1240—1245 (2004).
15) Cai W., Ebrahimnejad A., Chen K., Cao Q., Li Z. B., Tice D. A., Chen X., *Eur. J. Nucl. Med. Mol. Imaging*, **34**, 2024—2036 (2007).
16) Stabin M. G., Sparks R. B., Crowe E., *J. Nucl. Med.*, **46**, 1023—1027 (2005).
17) Matsumura Y., Maeda H., *Cancer Res.*, **46**, 6387—6392 (1986).
18) Ekblad T., Tran T., Orlova A., Widstrom C., Feldwisch J., Abrahmsen L., Wennborg A., Karlstrom A. E., Tolmachev V., *Eur. J. Nucl. Med. Mol. Imaging*, **35**, 2245—2255 (2008).
19) Kiratli P. O., Aksoy T., Bozkurt M. F., Orhan D., *Ann. Nucl. Med.*, **23**, 97—105 (2009).
20) Holliger P., Hudson P. J., *Nat. Biotechnol.*, **23**, 1126—1136 (2005).
21) Wong J. Y., Chu D. Z., Williams L. E., Yamauchi D. M., Ikle D. N., Kwok C. S., Liu A., Wilczynski S., Colcher D., Yazaki P. J., Shively J. E., Wu A. M., Raubitschek A. A., *Clin. Cancer Res.*, **10**, 5014—5021 (2004).
22) Ueda M., Iida Y., Mukai T., Mamede M., Ishizu K., Ogawa M., Magata Y., Konishi J., Saji H., *Ann. Nucl. Med.*, **18**, 337—344 (2004).
23) Wagner S., Breyholz H. J., Faust A., Holtke C., Levkau B., Schober O., Schafers M., Kopka K., *Curr. Med. Chem.*, **13**, 2819—2838 (2006).
24) Wagner S., Breyholz H. J., Holtke C., Faust A., Schober O., Schafers M., Kopka K., *Appl. Radiat. Isot.*, **67**, 606—610 (2009).
25) Ogawa K., Mukai T., Asano D., Kawashima H., Kinuya S., Shiba K., Hashimoto K., Mori H., Saji H., *J. Nucl. Med.*, **48**, 122—127 (2007).
26) Medhurst S. J., Walker K., Bowes M., Kidd B. L., Glatt M., Muller M., Hattenberger M., Vaxelaire J., O'Reilly T., Wotherspoon G., Winter J., Green J., Urban L., *Pain*, **96**, 129—140 (2002).
27) Chew E. C., *Experientia*, **32**, 1192—1194 (1976).
28) Saitoh J., Sakurai H., Suzuki Y., Muramatsu H., Ishikawa H., Kitamoto Y., Akimoto T., Hasegawa M., Mitsuhashi N., Nakano T., *Int. J. Radiat. Oncol. Biol. Phys.*, **54**, 903—909 (2002).
29) Masunaga S., Ono K., Suzuki M., Kinashi Y., Takagaki M., *Int. J. Radiat. Oncol. Biol. Phys.*, **49**, 1361—1368 (2001).
30) Wang X., Ma D., Keski-Oja J., Pei D., *J. Biol. Chem.*, **279**, 9331—9336 (2004).
31) Itoh Y., Takamura A., Ito N., Maru Y., Sato H., Suenaga N., Aoki T., Seiki M., *EMBO J.*, **20**, 4782—4793 (2001).
32) Sakai K., Yokote H., Murakami-Murofushi K., Tamura T., Saijo N., Nishio K., *Cancer Sci.*, **98**, 1498—1503 (2007).
33) Ren X. H., Peng X. D., Wu X. P., Liao E. Y., Sun Z. Q., *Clin. Chim. Acta*, **390**, 44—48 (2008).
34) Toth M., Hernandez-Barrantes S., Osenkowski P., Bernardo M. M., Gervasi D. C., Shimura Y., Meroueh O., Kotra L. P., Galvez B. G., Arroyo A. G., Mobashery S., Fridman R., *J. Biol. Chem.*, **277**, 26340—26350 (2002).

Biochemical and Biophysical Research Communications xxx (2009) xxx–xxx

Contents lists available at ScienceDirect

Biochemical and Biophysical Research Communications

journal homepage: www.elsevier.com/locate/ybbrc

GLP-1 receptor antagonist as a potential probe for pancreatic β-cell imaging

Eri Mukai [a,b], Kentaro Toyoda [a], Hiroyuki Kimura [c], Hidekazu Kawashima [d], Hiroyuki Fujimoto [a,b], Masashi Ueda [e], Takashi Temma [c], Konomu Hirao [f], Kenji Nagakawa [f], Hideo Saji [c], Nobuya Inagaki [a,g,*]

[a] Department of Diabetes and Clinical Nutrition, Graduate School of Medicine, Kyoto University, Kyoto, Japan
[b] Japan Association for the Advancement of Medical Equipment, Tokyo, Japan
[c] Department of Patho-Functional Bioanalysis, Graduate School of Pharmaceutical Sciences, Kyoto University, Kyoto, Japan
[d] Department of Diagnostic Imaging and Nuclear Medicine, Graduate School of Medicine, Kyoto University, Kyoto, Japan
[e] Radioisotopes Research Laboratory, Kyoto University Hospital, Faculty of Medicine, Kyoto University, Kyoto, Japan
[f] Research & Development Division, Arkray, Inc., Kyoto, Japan
[g] CREST of Japan Science and Technology Cooperation (JST), Kyoto, Japan

ARTICLE INFO

Article history:
Received 2 September 2009
Available online xxxx

Keywords:
Glucagon-like peptide-1
Glucagon-like peptide-1 receptor
Exendin-4
Exendin(9-39)
β-Cell imaging
Islet imaging
Molecular imaging
β-Cell mass
Diabetes

ABSTRACT

We examined exendin(9-39), an antagonist of glucagon-like peptide-1 (GLP-1) receptor (GLP-1R), as a potential probe for imaging of pancreatic β-cells. To evaluate *in vitro* receptor specificity, binding assay was performed using dispersed mouse islet cells. Binding assay showed competitive inhibition of [^{125}I]BH-exendin(9-39) binding by non-radioactive exendin(9-39). To assess *in vivo* selectivity, the biodistribution was evaluated by intravenous administration of [^{125}I]BH-exendin(9-39) to mice. Radioactivity of harvested pancreas reached highest levels at 60 and 120 min among organs examined except lung. Pre-administration of excess non-radioactive exendin(9-39) remarkably and specifically blocked the radioactivity of pancreas. After [^{125}I]BH-exendin(9-39) injection into transgenic mice with pancreatic β-cells expressing GFP, fluorescent and radioactive signals of sections of pancreas were evaluated with an image analyzer. Imaging analysis showed that the fluorescent GFP signals and the radioactive signals were correspondingly located. Thus, the GLP-1R antagonist exendin(9-39) may serve as a useful probe for pancreatic β-cell imaging.

Introduction

Type 1 diabetes is an autoimmune disease in which the pancreatic β-cells are almost destroyed, which leads to loss of endogenous insulin secretion. Insulin therapy is therefore required for survival in subjects with type 1 diabetes [1]. Type 2 diabetes is characterized by impaired insulin secretion and insulin resistance, and the pathogenesis is well known to be dependent on a reduction in β-cell function [2]. While a decrease in β-cell mass has been reported in American and Asian type 2 diabetic subjects compared with non-diabetic subjects [3–5], the decrease is small at onset in European subjects, suggesting that the decrease might occur only after onset of the disease [6]. It is therefore unknown whether a decrease in β-cell mass contributes to the development of hyperglycemia that leads to type 2 diabetes. Thus, accurately measuring changes in β-cell mass *in vivo* during diabetes progression is important not only for understanding the pathogenesis but also for facilitating early diagnosis and developing improved treatments for both type 1 and type 2 diabetes.

* Corresponding author. Address: Department of Diabetes and Clinical Nutrition, Graduate School of Medicine, Kyoto University, 54 Shogoin Kawahara-cho, Sakyo-tu, Kyoto 606-8507, Japan. Fax: +81 75 771 6601.
E-mail address: inagaki@metab.kuhp.kyoto-u.ac.jp (N. Inagaki).

0006-291X/$ - see front matter © 2009 Published by Elsevier Inc.
doi:10.1016/j.bbrc.2009.09.014

However, it is difficult to identify islets ranging in size from 50–500 μm in diameter and scattered throughout the pancreas, which is surrounded by abdominal organs. To quantify β-cell mass non-invasively, appropriate probes that can specifically bind to pancreatic β-cells are required. There are previous reports using probes targeting the proteins in β-cells, including sulfonylurea receptor 1 (SUR1) and monoamine transporter 2 (VMAT2) for positron emission tomography (PET) imaging [7]. However, ideal probes for accurate and non-invasive imaging for pancreatic β-cells have not yet been developed.

Glucagon-like peptide 1 (GLP-1) is the incretin peptide released from the intestine in response to nutrient ingestion to augment glucose-induced insulin secretion from pancreatic β-cells through binding to the GLP-1 receptor (GLP-1R) [8,9]. Since GLP-1R is expressed highly in islets, especially on β-cells in pancreas, the ligands of GLP-1R might well be ideal probes for pancreatic β-cell imaging. Because native GLP-1 is degraded rapidly by dipeptidyl peptidase-IV (DPP-IV) distributed throughout the body, DPP-IV-resistant agonistic or antagonistic ligands of GLP-1R [10,11] are preferable to GLP-1 for use as an imaging probe.

In the present study, specific imaging of pancreatic β-cells targeting GLP-1R was evaluated using its antagonist, exendin(9-39), radiolabeled with [^{125}I]-Bolton-Hunter reagent at lysine residues.

Please cite this article in press as: E. Mukai et al., GLP-1 receptor antagonist as a potential probe for pancreatic β-cell imaging, Biochem. Biophys. Res. Commun. (2009), doi:10.1016/j.bbrc.2009.09.014

Materials and methods

Radiolabeling of exendin(9-39). [^{125}I]-Bolton-Hunter-labeled exendin(9-39) ([^{125}I]-BH exendin(9-39)) was purchased from Perkin-Elmer (Waltham, MA).

Animals. Six-week-old male ddY mice were obtained from Shimizu Co. (Kyoto, Japan). Transgenic mice expressing green fluorescent protein (GFP) under control of the mouse insulin I gene promoter (MIP) (MIP-GFP mice) were maintained on a C57BL/6 background [12]. Animal care and procedures were approved by the Animal Care Committee of Kyoto University.

Binding assay. The displacing effect of exendin(9-39) on GLP-1R binding was assessed using dispersed islet cells as described previously [13]. Pancreatic islets were isolated from male ddY mice by a collagenase digestion technique [14]. Isolated islets were dispersed using 0.05% trypsin/0.53 mM EDTA (Invitrogen, Carlsbad, CA) and PBS. Islet cells were incubated with [^{125}I]BH-exendin(9-39) (0.1 μCi) in 1 ml of buffer containing 20 mM Hepes (pH 7.4), 1 mM $MgCl_2$, 1 mg/ml bacitracin, and 1 mg/ml BSA for 1 h at room temperature in the presence of varying concentrations of non-radioactive exendin(9-39). Binding was terminated by rapid filtration through Whatman GF/C filters (24 mm) followed by washing three times with 5 ml of ice-cold PBS. The radioactivity of filters was measured in a γ-counter. Results were expressed as the percent radioactivity of bound [^{125}I]BH-exendin(9-39) that remained after addition of non-radioactive compound.

Biodistribution experiments. Biodistribution studies of [^{125}I]BH-exendin(9-39) were performed in male ddY mice. [^{125}I]BH-exendin(9-39) (1 μCi) was administered by tail vein injection. At 15, 30, 60, and 120 min after administration, the mice were sacrificed by exsanguination under anesthesia. Selected organs and blood

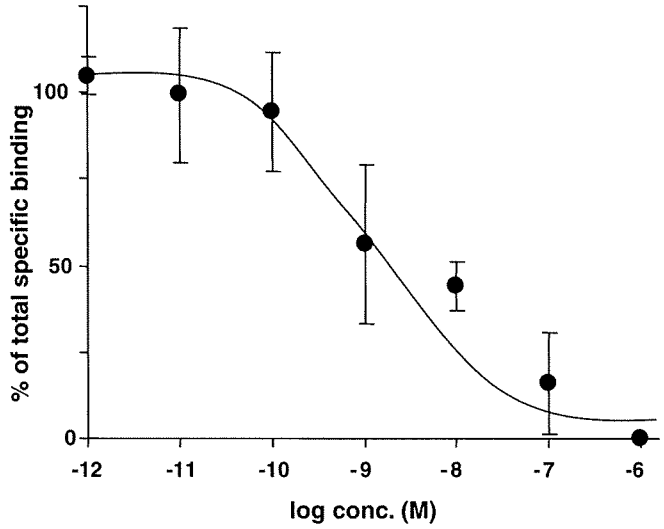

Fig. 1. Binding assay analysis of [^{125}I]BH-exendin(9-39) using mouse pancreatic islet cells. Competitive inhibition of [^{125}I]BH-exendin(9-39) binding by non-radioactive exendin(9-39) is shown. Values are expressed as means ± SD of the percent radioactivity of bound [^{125}I]BH-exendin(9-39) that remained after addition of indicated concentrations of non-radioactive exendin(9-39) (n = 4).

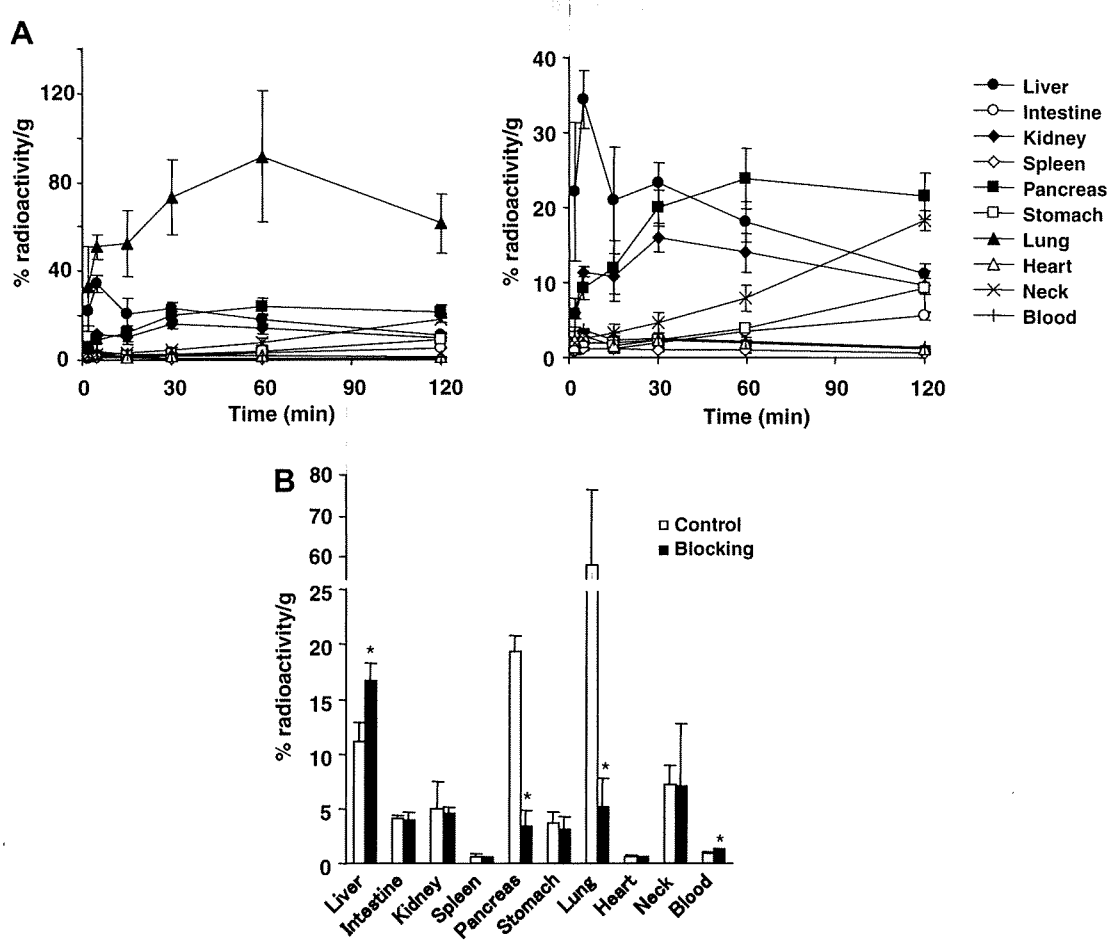

Fig. 2. Tissue distribution of [^{125}I]BH-exendin(9-39) in mice. (A) Time course of tissue distribution of [^{125}I]BH-exendin(9-39). Right graph shows tissue distribution without lung. (B) Blocking of tissue distribution at 120 min after [^{125}I]BH-exendin(9-39) injection by pre-administration of excess non-radioactive exendin(9-39). Values are expressed as means ± SD of the percent radioactivity of injected [^{125}I]BH-exendin(9-39) per gram of organ weight (n = 5). $^{*}P < 0.001$ vs. control.

Please cite this article in press as: E. Mukai et al., GLP-1 receptor antagonist as a potential probe for pancreatic β-cell imaging, Biochem. Biophys. Res. Commun. (2009), doi:10.1016/j.bbrc.2009.09.014

were harvested and weighed, and the radioactivities were measured with a γ-counter. In a blocking study, excess non-radioactive exendin(9-39) (50 μg) in 100 μl of saline was administered 30 min before the [^{125}I]BH-exendin(9-39) injection. Results were expressed as percent radioactivity of injected [^{125}I]BH-exendin(9-39) per gram of organ weight.

Two-dimensional imaging analysis. After intravenous administration of [^{125}I]BH-exendin(9-39) to male MIP-GFP mice, the pancreas was harvested and cut in several pieces. Each piece was put on slide glass and pressed with a cover glass. Signals of fluorescence and radioactivity (autoradiography) of sections of pancreas were evaluated with an image analyzer (Typhoon 9410; GE Healthcare, Buckinghamshire, UK). The fluorescent and radioactive intensity of each section was analyzed with ImageQuant TL software with resolution of 25 and 10 μm per pixel, respectively (GE Healthcare).

Statistical analysis. Data are expressed as means ± SD. Statistical significance of difference was evaluated by unpaired alternate Welch *t* test. $P < 0.05$ was considered significant.

Results and discussion

We first examined binding specificity of exendin(9-39) to pancreatic β-cell membrane *in vitro*. Binding assay analysis using mouse pancreatic islet cells showed competitive inhibition of [^{125}I]BH-exendin(9-39) binding by non-radioactive exendin(9-39) with a $\log IC_{50}$ of -8.84 ± 0.18, similarly to the findings in a previous report [15], indicating that exendin(9-39) binds to those cells specifically (Fig. 1).

To examine selectivity of exendin(9-39) to pancreas *in vivo*, we performed biodistribution studies in mice. Radioactivities of selected organs were measured 15, 30, 60, and 120 min after intravenous administration of [^{125}I]BH-exendin(9-39) (1 μCi). The radioactivity of lung was highest at each time point (Fig. 2A, left panel). Radioactivity of pancreas increased with time and was highest at 60 and 120 min among organs examined excepting lung, and rapid and high binding by liver was observed (Fig. 2A, right panel). To determine whether the binding was specific, we performed blocking study. Pre-administration of excess non-radioactive exendin(9-39) (50 μg) significantly blocked the radioactivities of pancreas and lung to 17.8% and 8.8% of control, respectively, 120 min after [^{125}I]BH-exendin(9-39) injection (Fig. 2B), demonstrating that [^{125}I]BH-exendin(9-39) specifically binds to its receptor in these organs. The binding in other organs such as liver was not blocked by excess non-radioactive exendin(9-39).

To confirm high binding of exendin(9-39) in β-cells, we performed [^{125}I]BH-exendin(9-39) injection in MIP-GFP mice specifically expressing GFP in pancreatic β-cells and imaging analysis of sections of the pancreas removed 60 or 120 min after [^{125}I]BH-exendin(9-39) injection. As shown in Fig. 3A, fluorescent GFP signals were observed in the pancreatic sections of MIP-GFP mice with an image analyzer. Localization of the detected radioactive signals corresponded well to that of the GFP signals, indicating specific high binding of exendin(9-39) in pancreatic β-cells. The intensity of the fluorescent signals of each section also correlated with that of the radioactive signals (Fig. 3B).

Studies for detecting β-cell mass have been performed using probes targeting various β-cell-specific molecules, among which GLP-1R appears promising [7]. *In vivo* imaging of GLP-1R-positive tissues using diethylenetriaminepentaacetic acid (DTPA)-conjugated exendin-4, the GLP-1R agonist, was recently reported [16]. The biodistribution examinations showed its specific binding not only to pancreas and lung but also to stomach. Although pancreas and lung as well as pituitary and adrenals were detected in single photon emission computed tomography (SPECT) imaging, it was not determined whether the probe was confined to β-cells due to the low resolution of the imaging apparatus. In the present study, we found that exendin(9-39), an antagonistic ligand of GLP-1R, has high specificity not only to pancreas but also to β-cells in pancreas, suggesting that β-cell mass can be evaluated. High binding of the probe in lung, as previously reported [16], does not affect analysis of islets because lung is an extra-abdominal organ, for which imaging such as SPECT is required.

A better understanding of the relationship between β-cell mass, β-cell function, and glucose homeostasis by precise measurement of β-cell mass should provide important information on not only for early diagnosis and treatment but also for development of new therapies for intervention strategies. Several tests are presently available for evaluation of β-cell function [17]. In contrast,

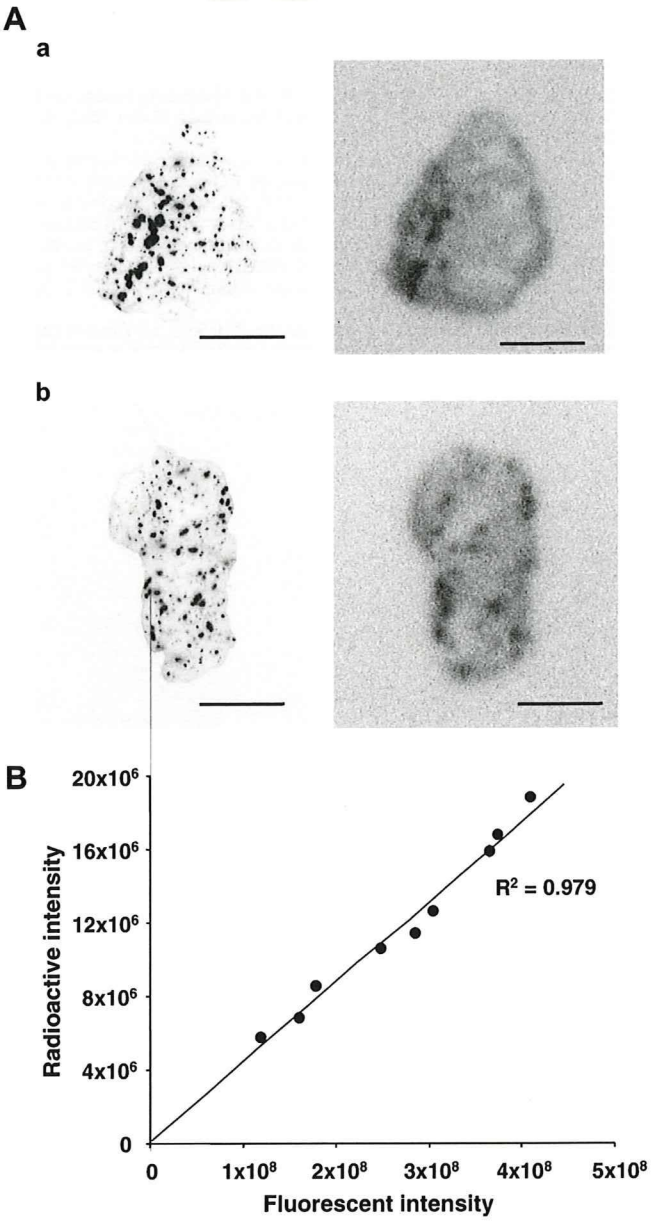

Fig. 3. Imaging analysis of pancreas sections of [^{125}I]BH-exendin(9-39)-injected MIP-GFP mice. (A) Representative fluorescent signals (left panels) and radioactive signals (right panels) of pancreas sections at 60 min (a) and 120 min (b) after [^{125}I]BH-exendin(9-39) injection. Bars represent 1 cm. (B) Correlation of the fluorescent and radioactive intensity. The signal intensity in whole area of each of the nine sections of pancreas harvested 120 min after [^{125}I]BH-exendin(9-39) injection was analyzed with ImageQuant TL software.

Please cite this article in press as: E. Mukai et al., GLP-1 receptor antagonist as a potential probe for pancreatic β-cell imaging, Biochem. Biophys. Res. Commun. (2009), doi:10.1016/j.bbrc.2009.09.014

measurement of β-cell mass is presently possible only by autopsy. It has recently been reported that antagonistic probes as well as agonistic probes are useful for molecular imaging by targeting peptide receptors [18]. In the present study, we demonstrate for the first time that the GLP-1R antagonist exendin(9-39) is a potential probe for the imaging of pancreatic β-cells.

Acknowledgments

We thank Dr. M. Hara, University of Chicago, for generously providing us transgenic MIP-GFP mice. This work was supported by a Research Grant on Nanotechnical Medicine from the Ministry of Health, Labour, and Welfare of Japan, and by Scientific Research Grants from the Ministry of Education, Culture, Sports, Science, and Technology of Japan, and also by Kyoto University Global COE Program "Center for Frontier Medicine".

References

[1] W.V. Tamborlane, W. Bonfig, E. Boland, Recent advances in treatment of youth with type 1 diabetes: better care through technology, Diabet. Med. 18 (2001) 864–870.
[2] L. Groop, Pathogenesis of type 2 diabetes: the relative contribution of insulin resistance and impaired insulin secretion, Int. J. Clin. Pract. Suppl. (2000) 3–13.
[3] H. Sakuraba, H. Mizukami, N. Yagihashi, R. Wada, C. Hanyu, S. Yagihashi, Reduced beta-cell mass and expression of oxidative stress-related DNA damage in the islet of Japanese type II diabetic patients, Diabetologia 45 (2002) 85–96.
[4] A.E. Butler, J. Janson, S. Bonner-Weir, R. Ritzel, R.A. Rizza, P.C. Butler, Beta-cell deficit and increased beta-cell apoptosis in humans with type 2 diabetes, Diabetes 52 (2003) 102–110.
[5] K.H. Yoon, S.H. Ko, J.H. Cho, J.M. Lee, Y.B. Ahn, K.H. Song, S.J. Yoo, M.I. Kang, B.Y. Cha, K.W. Lee, H.Y. Son, S.K. Kang, H.S. Kim, I.K. Lee, S. Bonner-Weir, Selective beta-cell loss and alpha-cell expansion in patients with type 2 diabetes mellitus in Korea, J. Clin. Endocrinol. Metab. 88 (2003) 2300–2308.
[6] J. Rahier, Y. Guiot, R.M. Goebbels, C. Sempoux, J.C. Henquin, Pancreatic beta-cell mass in European subjects with type 2 diabetes, Diabetes Obes. Metab. 10 (Suppl. 4) (2008) 32–42.
[7] S. Schneider, Efforts to develop methods for in vivo evaluation of the native beta-cell mass, Diabetes Obes. Metab. 10 (Suppl. 4) (2008) 109–118.
[8] L.L. Baggio, D.J. Drucker, Biology of incretins: GLP-1 and GIP, Gastroenterology 132 (2007) 2131–2157.
[9] J.J. Holst, The physiology of glucagon-like peptide 1, Physiol. Rev. 87 (2007) 1409–1439.
[10] J. Eng, W.A. Kleinman, L. Singh, G. Singh, J.P. Raufman, Isolation and characterization of exendin-4, an exendin-3 analogue, from *Heloderma suspectum* venom. Further evidence for an exendin receptor on dispersed acini from guinea pig pancreas, J. Biol. Chem. 267 (1992) 7402–7405.
[11] R. Goke, H.C. Fehmann, T. Linn, H. Schmidt, M. Krause, J. Eng, B. Goke, Exendin-4 is a high potency agonist and truncated exendin-(9-39)-amide an antagonist at the glucagon-like peptide 1-(7-36)-amide receptor of insulin-secreting beta-cells, J. Biol. Chem. 268 (1993) 19650–19655.
[12] M. Hara, X. Wang, T. Kawamura, V.P. Bindokas, R.F. Dizon, S.Y. Alcoser, M.A. Magnuson, G.I. Bell, Transgenic mice with green fluorescent protein-labeled pancreatic beta-cells, Am. J. Physiol. Endocrinol. Metab. 284 (2003) E177–E183.
[13] E. Mukai, H. Ishida, S. Kato, Y. Tsuura, S. Fujimoto, A. Ishida-Takahashi, M. Horie, K. Tsuda, Y. Seino, Metabolic inhibition impairs ATP-sensitive K+ channel block by sulfonylurea in pancreatic beta-cells, Am. J. Physiol. 274 (1998) E38–E44.
[14] R. Sutton, M. Peters, P. McShane, D.W. Gray, P.J. Morris, Isolation of rat pancreatic islets by ductal injection of collagenase, Transplantation 42 (1986) 689–691.
[15] S. Al-Sabah, D. Donnelly, A model for receptor-peptide binding at the glucagon-like peptide-1 (GLP-1) receptor through the analysis of truncated ligands and receptors, Br. J. Pharmacol. 140 (2003) 339–346.
[16] M. Gotthardt, G. Lalyko, J. van Eerd-Vismale, B. Keil, T. Schurrat, M. Hower, P. Laverman, T.M. Behr, O.C. Boerman, B. Goke, M. Behe, A new technique for in vivo imaging of specific GLP-1 binding sites: first results in small rodents, Regul. Pept. 137 (2006) 162–167.
[17] S.E. Kahn, D.B. Carr, M.V. Faulenbach, K.M. Utzschneider, An examination of beta-cell function measures and their potential use for estimating beta-cell mass, Diabetes Obes. Metab. 10 (Suppl. 4) (2008) 63–76.
[18] M. Schottelius, H.J. Wester, Molecular imaging targeting peptide receptors, Methods 48 (2009) 161–177.

Please cite this article in press as: E. Mukai et al., GLP-1 receptor antagonist as a potential probe for pancreatic β-cell imaging, Biochem. Biophys. Res. Commun. (2009), doi:10.1016/j.bbrc.2009.09.014

Ann Nucl Med
DOI 10.1007/s12149-009-0319-4

ORIGINAL ARTICLE

Preparation and evaluation of $^{186/188}$Re-labeled antibody (A7) for radioimmunotherapy with rhenium(I) tricarbonyl core as a chelate site

Kazuma Ogawa · Hidekazu Kawashima · Seigo Kinuya · Kazuhiro Shiba · Masahisa Onoguchi · Hiroyuki Kimura · Kazuyuki Hashimoto · Akira Odani · Hideo Saji

Received: 16 June 2009 / Accepted: 9 September 2009

Abstract
Objective Rhenium is one of the most valuable elements for internal radiotherapy because ^{186}Re and ^{188}Re have favorable physical characteristics. However, there are problems when proteins such as antibodies are used as carriers of $^{186/188}$Re. Labeling methods that use bifunctional chelating agents such as MAG3 require the conjugation of the $^{186/188}$Re complex to protein after radiolabeling with the bifunctional chelating agent. These processes are complicated. Therefore, we planned the preparation by a simple method and evaluation of a stable $^{186/188}$Re-labeled antibody. For this purpose, we selected $^{186/188}$Re(I) tricarbonyl complex as a chelating site. In this study, A7 (an IgG1 murine monoclonal antibody) was used as a model protein. $^{186/188}$Re-labeled A7 was prepared by directly reacting a $^{186/188}$Re(I) tricarbonyl precursor, $[^{186/188}Re(CO)_3(H_2O)_3]^+$, with A7. We then compared the biodistribution of $^{186/188}$Re-labeled A7 in tumor-bearing mice with ^{125}I-labeled A7.
Methods For labeling A7, $[^{186/188}Re(CO)_3(H_2O)_3]^+$ was prepared according to a published procedure. $^{186/188}$Re-labeled A7 ($^{186/188}$Re-$(CO)_3$-A7) was prepared by reacting $[^{186/188}Re(CO)_3(H_2O)_3]^+$ with A7 at 43°C for 2 h. Biodistribution experiments were performed by the intravenous administration of $^{186/188}$Re-$(CO)_3$-A7 solution into tumor-bearing mice.
Results ^{186}Re-$(CO)_3$-A7 and ^{188}Re-$(CO)_3$-A7 were prepared with radiochemical yields of 23 and 28%, respectively. After purification with a PD-10 column, $^{186/188}$Re-$(CO)_3$-A7 showed a radiochemical purity of over 95%. In biodistribution experiments, 13.1 and 13.2% of the injected dose/g of ^{186}Re-$(CO)_3$-A7 and ^{188}Re-$(CO)_3$-A7, respectively, accumulated in the tumor at 24-h postinjection, and the tumor-to-blood ratios were over 2.0 at the same time point. Meanwhile, uptake of ^{125}I-A7 in the tumor was almost the same as that of $^{186/188}$Re-$(CO)_3$-A7 at 24-h postinjection. Blood clearances of $^{186/188}$Re-$(CO)_3$-A7 were faster than those of ^{125}I-A7.
Conclusion $^{186/188}$Re-labeled A7 showed high uptakes in the tumor. However, further modification of the labeling method would be necessary to improve radiochemical yields and their biodistribution.

Keywords Rhenium · Radioimmunotherapy · Antibody · Tricarbonyl

K. Ogawa (✉) · A. Odani
Graduate School of Natural Science and Technology, Kanazawa University, Kakuma-machi, Kanazawa 920-1192, Japan
e-mail: kogawa@p.kanazawa-u.ac.jp

K. Ogawa · K. Shiba
Advanced Science Research Center, Kanazawa University, Kanazawa, Japan

H. Kawashima
Kyoto University Hospital, Kyoto, Japan

S. Kinuya · M. Onoguchi
Graduate School of Medical Sciences, Kanazawa University, Kanazawa, Japan

H. Kimura · H. Saji
Graduate School of Pharmaceutical Sciences, Kyoto University, Kyoto, Japan

K. Hashimoto
Japan Atomic Energy Agency, Tokai-mura, Ibaraki, Japan

Introduction

Radioimmunotherapy with radiolabeled monoclonal antibodies (mAb) has great potential to be a good treatment

Published online: 17 November 2009